Quaternary tectonic evolution of the Pamir-Tian Shan convergence zone, Northwest China

Jessica Ann Thompson Jobe[1,2] (iD), Tao Li[3] (iD), Jie Chen[4] (iD), Douglas W. Burbank[1] (iD), and Aaron Bufe[1,5] (iD)

[1]Department of Earth Science, University of California, Santa Barbara, California, USA, [2]Institute of Tectonic Studies, Department of Geological Sciences, University of Texas at El Paso, El Paso, Texas, USA, [3]School of Earth Science and Engineering, Sun Yat-Sen University, Guangzhou, China, [4]State Key Laboratory of Earthquake Dynamics, Institute of Geology, China Earthquake Administration, Beijing, China, [5]Now at GFZ German Research Center for Geosciences, Potsdam, Germany

Abstract The Pamir-Tian Shan collision zone in the western Tarim Basin, northwest China, formed from rapid and ongoing convergence in response to the Indo-Eurasian collision. The arid landscape preserves suites of fluvial terraces crossing structures active since the late Neogene that create fault and fold scarps recording Quaternary deformation. Using geologic and geomorphic mapping, differential GPS surveys of deformed terraces, and optically stimulated luminescence dating, we create a synthesis of the active structures that delineate the timing, rate, and migration of Quaternary deformation during ongoing convergence. New deformation rates on eight faults and folds, when combined with previous studies, highlight the spatial and temporal patterns of deformation within the Pamir-Tian Shan convergence zone during the Quaternary. Terraces spanning ~130 to ~8 ka record deformation rates between ~0.1 and 5.6 mm/yr on individual structures. In the westernmost Tarim Basin, where the Pamir and Tian Shan are already juxtaposed, the fastest rates occur on actively deforming structures at the interface of the Pamir-Tian Shan orogens. Farther east, as the separation between the Pamir-Tian Shan orogens increases, the deformation has not been concentrated on a single structure, but rather has been concurrently distributed across a zone of faults and folds in the Kashi-Atushi fold-and-thrust belt and along the NE Pamir margin, where shortening rates vary on individual structures during the Quaternary. Although numerous structures accommodate the shortening and the locus of deformation shifts during the Quaternary, the total shortening across the western Tarim Basin has remained steady and approximately matches the current geodetic rate of 6–9 mm/yr.

1. Introduction

Large earthquakes and high seismic risk are commonly thought to be focused near the leading edge of contractional mountain ranges, where critical wedge theory and traditional conceptual models of orogens predict faults to be most active [*Dahlstrom*, 1970]. In these models, thrust faults form sequentially as they encroach on the foreland, with slip on a previous fault ceasing as a new frontal fault forms [*Armstrong and Oriel*, 1965; *Dahlstrom*, 1970]. Alternative models, based on modern seismicity and high-resolution GPS data, suggest deformation may be distributed across an orogeny and out-of-sequence faulting [*Kao*, 2000] and hinterland deformation [*Seeber et al.*, 1981] are necessary to maintain a critically tapered wedge [e.g., *Dahlen et al.*, 1984; *Dahlen*, 1990]. Most studies have focused on characterizing the leading edge of an orogen [*Lave and Avouac*, 2000; *Husson et al.*, 2004; *McClay et al.*, 2004], with relatively few studies assessing both hinterland and foreland deformation [*Burbank and Reynolds*, 1984]. Those studies that do assess multiple structures commonly focus on longer timescales (i.e., million-year timescales) [*Jordan et al.*, 1993; *Coutand et al.*, 2002; *Mugnier et al.*, 2004]. Thus, Quaternary slip rates on structures and the partitioning of active deformation across an orogenic wedge remain unknown in most collisional systems, despite the fact that these data provide valuable input for assessments for seismic hazards and risk [*Murphy et al.*, 2013].

The present-day partitioning of deformation in convergent orogens is commonly determined using modern GPS [*McCaffrey et al.*, 2000; *Nilforoushan et al.*, 2003; *Reilinger et al.*, 2006], interferometric synthetic aperture radar (InSAR) [*Wright*, 2004; *Goode et al.*, 2011; *Cavalié and Jónsson*, 2014; *He et al.*, 2015], and the seismic record [*Negredo et al.*, 2007; *Schurr et al.*, 2014], which may also be integrated with geology and geomorphology [*Seeber and Pecher*, 1998; *Siame et al.*, 2005; *Engdahl et al.*, 2006; *Fu et al.*, 2010]. However, these techniques only reveal strain partitioning on decadal timescales. Furthermore, the patterns of recent seismicity

and deformation do not always correlate with mapped Neogene or Quaternary faults and folds [*Siame et al.*, 2005]. Thus, these historical records lack the temporal resolution to fully understand how an orogen has evolved through the Quaternary and link longer timescales (million year) to the modern day.

In Central Asia, the use of historical records and remote sensing has revealed the present-day partitioning of deformation between strike-slip faults on the margins of the Pamir [*Fu et al.*, 2010; *Mohadjer et al.*, 2010; *Ischuk et al.*, 2013; *Zhou et al.*, 2016], intracontinental subduction of the Eurasian lithosphere under the Pamir/Indian lithosphere [*Negredo et al.*, 2007; *Sobel et al.*, 2013; *Schurr et al.*, 2014], and distributed deformation within the Tian Shan range [*Goode et al.*, 2011]. In addition to modern geodetic studies, the Quaternary activity of individual faults and folds along the southern Tian Shan [*Chen et al.*, 2002, 2005; *Hubert-Ferrari*, 2005; *Chen et al.*, 2007a; *Daëron et al.*, 2007; *Hubert-Ferrari et al.*, 2007; *Heermance et al.*, 2008; *Huang et al.*, 2014] and northeastern Pamir [*Li et al.*, 2012, 2013, 2015a] has been studied in detail. Furthermore, recent work in the interior of the Kyrgyz Tian Shan focused on determining shortening rates on a suite of faults and folds [*Thompson et al.*, 2002; *Goode et al.*, 2014] and compared the regional late Quaternary deformation rates to modern geodetic rates, with good agreement over the two timescales. Although several of these studies illuminate temporal patterns of deformation on a single structure in the western Tarim Basin, detailed records of spatial and temporal strain partitioning along the margins of the ranges, and importantly, where two orogens are colliding, remain uncommon [*Thompson et al.*, 2002; *Li et al.*, 2012; *Goode et al.*, 2014].

This study presents new Quaternary shortening rates across eight faults and folds along the margins of the Tian Shan and NE Pamir orogens in the western Tarim Basin. These structures commonly preserve multiple flights of terraces that permit quantification of the Quaternary spatiotemporal evolution of the deformation as the collision between the Tian Shan and Pamir progressed. We integrate our data with previous recent work in the region [*Scharer et al.*, 2004; *Chen et al.*, 2005; *Heermance et al.*, 2008; *Li*, 2012; *Li et al.*, 2012, 2013, 2015a, 2015b; *Thompson*, 2013; *Yang*, 2013; *Bufe et al.*, 2017a, 2017b] to reconstruct Quaternary deformation patterns across the western Tarim Basin.

2. Geology of the NE Pamir and Tian Shan

In northwest China, the western Tarim Basin lies between the Pamir and Tian Shan orogens. To the southwest, the Pamir salient is the northwestern continuation of the Tibetan Plateau (Figure 1) and was formed during the Indo-Eurasian collision [*Burtman and Molnar*, 1993]. Peaks higher than 7000 m form the northeastern edge of the Pamir. To the north of the Tarim Basin, the Tian Shan stretch over 2000 km from Uzbekistan in the west to China in the east and span 300–500 km in width. The peaks of the Tian Shan also exceed 7000 m in the range interior. At the edge of the Pamir Plateau and the Tian Shan, the topography drops several thousand meters into foreland basins that constitute the western Tarim Basin.

The Pamir orogen is an amalgamation of terranes that are the along-strike equivalents of tectonic terranes in the Himalaya and Tibetan Plateau that were accreted to the southern front of Eurasia during the Mesozoic and Paleozoic [*Burtman and Molnar*, 1993; *Robinson et al.*, 2004; *Schwab et al.*, 2004]. During the Cenozoic, the Pamir has indented northward ~300 km relative to stable Eurasia and has accommodated 300–900 km of ~N-S crustal shortening. This shortening occurred through significant crustal thickening and thrusting on its northern margins [*Burtman and Molnar*, 1993] and in the interior of the plateau [*Stearns et al.*, 2015], strike-slip movement along a series of sinistral and dextral strike-slip faults on the eastern and western margins [*Frisch et al.*, 1994] (Figure 1), and intracontinental subduction of the Tian Shan beneath the Pamir along a southward-dipping subduction zone [*Burtman and Molnar*, 1993; *Negredo et al.*, 2007; *Sobel et al.*, 2013].

From the Miocene to the present, deformation along the northeastern margin of the Pamir has been focused on thrust faults bounding the plateau (Figures 1 and 2) [*Sobel and Dumitru*, 1997; *Sobel et al.*, 2011], faults and folds within the foreland basin [*Li et al.*, 2012, 2013; *Thompson et al.*, 2015], large strike-slip transfer systems on the eastern margin (the Kashgar-Yecheng Transfer System (KYTS), to the south of the area in Figure 1) [*Cowgill*, 2010; *Sobel et al.*, 2011; *Cao et al.*, 2013], and extensional domes on the plateau formed by gravitational collapse of overthickened crust (Kongur Extensional System (KES)) [*Robinson et al.*, 2004, 2007; *Amidon and Hynek*, 2010; *Sobel et al.*, 2011; *Cao et al.*, 2013a, 2013b; *Sobel et al.*, 2013; *Thiede et al.*, 2013]. At least four thrust faults crop out on the northeastern margin of the Pamir. The Main Pamir Thrust (MPT) is the
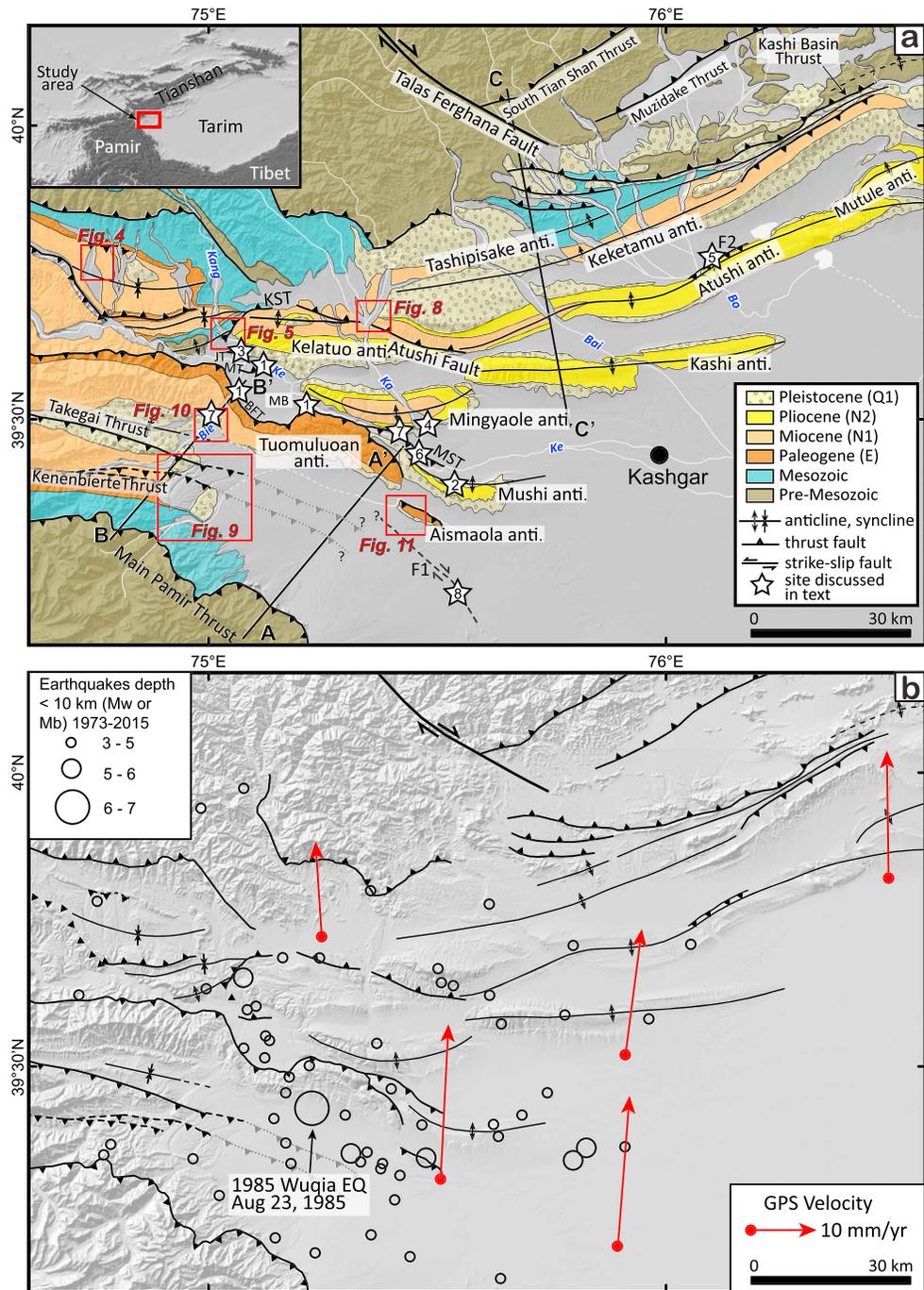
Figure 1. (a) Simplified geologic map of the western Tarim Basin. Inset map marks location in Central Asia. Stars mark locations of previous studies discussed in text. 1: *Li et al.* [2012]; 2: *Li et al.* [2013]; 3: *Li* [2012]; 4: *Li et al.* [2015a]; 5: *Shen et al.* [2001]; 6: *Yang* [2013]; 7: *Thompson* [2013]; and 8: *Fu et al.* [2010]. Map modified from *Li et al.* [2015a]. MB = Mayikake Basin, MST = Mingyaole South Thrust, JT = Jilegeyoute Thrust, KST = Kangsu South Thrust, MT = Mayikake Thrust, BFT = Bieertuokuoyi segment of the Pamir Frontal Thrust, F1 = unnamed Fault 1, F2 = unnamed Fault 2, Bie = Bieertuokuoyi River, Ke = Kezilesu River, Kang = Kangsu River, Bai = Baishikeremu River, Ka = Kalanggouluke River, and Bo = Boguzi River. (b) Hillshade derived from the 90 m SRTM DEM showing the major structures (symbols same as in Figure 1a), earthquake epicenters from 1973–2015, and the horizontal GPS velocity from *Zubovich et al.* [2010].
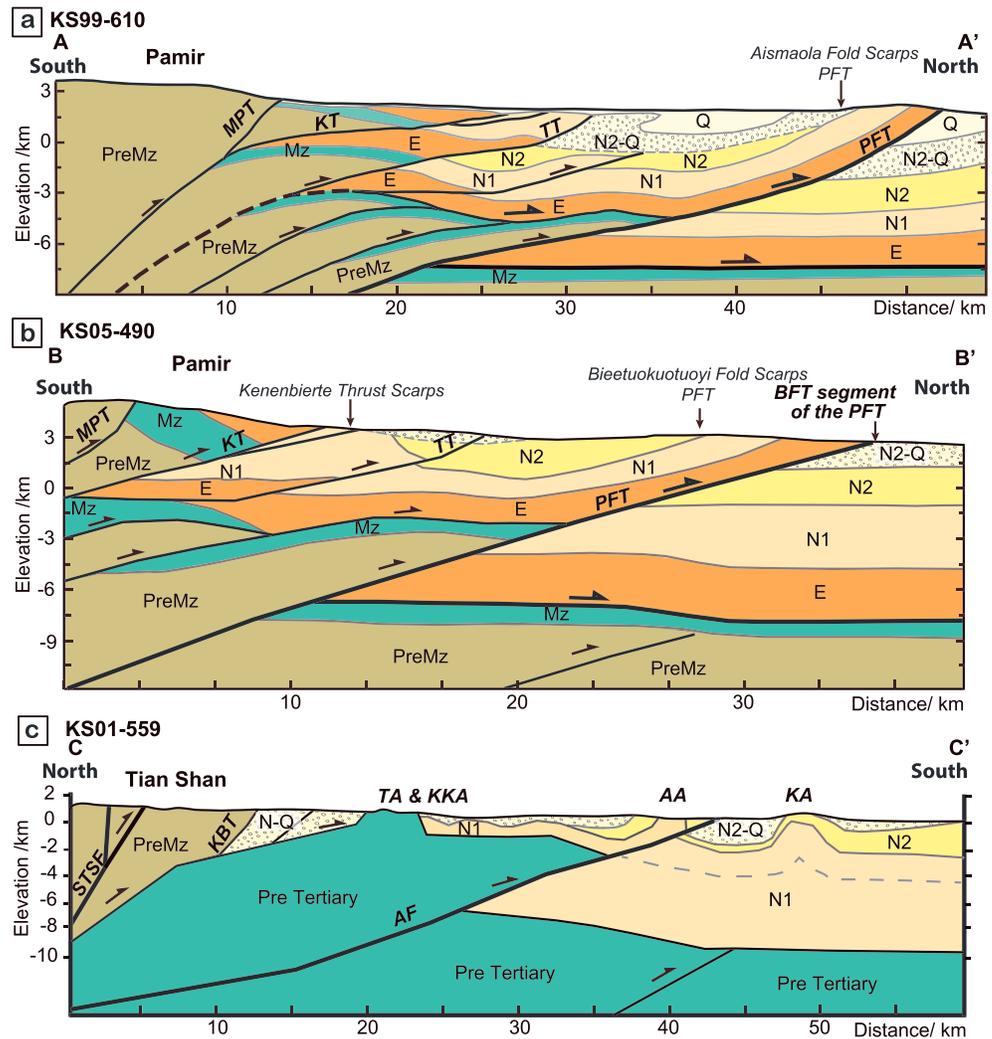
Figure 2. Interpreted seismic lines across the western Tarim Basin, illustrating the structures at depth. The locations of the seismic lines are shown in Figure 1. (a) line KS99–610 and (b) line KS05–490 across the NE Pamir margin. Modified from *Chen et al.* [2010] and *Cheng et al.* [2016]. Kenenbierte and Takegai Thrusts do not have a surface expression in Figure 2a and are likely covered by Quaternary alluvium. (c) line KS01-559 across the Kashi-Atushi fold-and-thrust belt, modified from *Heermance et al.* [2008]. Note Pre-Tertiary strata, instead of Mz and Pre-Mz strata, at depth. MPT = Main Pamir Thrust, KT = Kenenbierte Thrust, TT = Takegai Thrust, PFT = Pamir Frontal Thrust, BFT = Bieertuokuoyi segment of the PFT, TA = Tashipishake Anticline, KKA = Keketamu Anticline, AA = Atushi Anticline, KA = Kashi Anticline, and AF = Atushi Fault.

major fault separating the Pamir Plateau from the foreland (Figure 1). Based on detrital low-temperature thermochronology, the MPT initiated 25–18 Ma; however, the slip rate is inferred to have slowed during the late Miocene or Pliocene [*Sobel and Dumitru*, 1997; *Sobel et al.*, 2011]. Along the northern margin of the Pamir, shortening began during the Oligo-Miocene and continues to the present [*Arrowsmith and Strecker*, 1999; *Coutand et al.*, 2002]. Farther west, where the Pamir and Tian Shan are already juxtaposed, the collision began as late as the Mio-Pliocene [*Pavlis et al.*, 1997]. The Pamir Frontal Thrust (PFT), spatially separated from the MPT by ~30 km, is the northernmost structure of the Pamir (Figure 1). Based on magnetostratigraphy and cosmogenic burial dating of growth strata, the PFT initiated ~5–6 Ma [*Thompson et al.*, 2015]. The Kenenbierte Thrust (KT) and Takegai Thrust (TT) lie between the MPT and PFT, and may have initiated synchronously with, or earlier than, the PFT (Figure 1) [*Thompson et al.*, 2015].

To the north, the Tian Shan originally formed as a result of multiple collisional events in the Paleozoic and Mesozoic, yielding a complex deformation history [*Windley et al.*, 1990; *Hendrix et al.*, 1992; *Carroll et al.*, 1995; *Dumitru et al.*, 2001]. As a result of the Indo-Eurasian collision, the Tian Shan experienced diachronous uplift and exhumation that began between the late Oligocene and the late Miocene [*Hendrix et al.*, 1994; *Sobel and Dumitru*, 1997; *Charreau et al.*, 2006, 2009; *Sobel et al.*, 2006], with deformation propagating outward into the Tarim and Junggar Basins during the Miocene to Holocene [*Charreau et al.*, 2006; *Huang et al.*, 2006; *Sobel et al.*, 2006; *Hubert-Ferrari et al.*, 2007; *Heermance et al.*, 2008; *Charreau et al.*, 2009; *Huang et al.*, 2009].

During the Plio-Pleistocene, deformation in both the Tian Shan and the Pamir has continued to propagate into the western Tarim Basin (Figure 2), where it created a series of thrust faults and anticlines that obliquely impinge on each other, creating the Pamir-Tian Shan convergence zone [*Chen et al.*, 2002; *Scharer et al.*, 2004; *Chen et al.*, 2005; *Scharer et al.*, 2006; *Chen et al.*, 2007a; *Heermance et al.*, 2008; *Li et al.*, 2012, 2013, 2015b; *Thompson et al.*, 2015]. The Pamir Frontal Thrust has accommodated ~50 km of shortening (Figure 2a) [*Chen et al.*, 2010; *Cheng et al.*, 2016] since initiation ~5–6 Ma [*Thompson et al.*, 2015], resulting in an average shortening rate of ~10–12 mm/yr. Since 0.35 Ma, the PFT accommodates nearly all of the late Quaternary deformation along the northeast margin of the Pamir, with an average shortening rate of 6–9 mm/yr [*Li et al.*, 2012]. The Mushi and Mingyaole anticlines, two structures at the interface between the Pamir and Tian Shan (Loc. 2 and Loc. 4, Figure 1), initiated during the Quaternary [*Chen et al.*, 2005; *Li et al.*, 2013; *Thompson*, 2013]. Magnetostratigraphy and cosmogenic burial ages date initial growth strata on the Mingyaole anticline to ~1.6 Ma [*Chen et al.*, 2005; *Thompson*, 2013], with an average shortening rate between 1.1 and 1.9 mm/yr since fold initiation [*Li et al.*, 2015b]. A cosmogenic burial age from the Mushi anticline dates the initiation of the folding to $1.3^{+1.1}/_{-0.5}$ Ma [*Thompson*, 2013], although estimates based on the total shortening and late Quaternary shortening rate suggest the fold initiated ~0.5 Ma [*Li et al.*, 2013]. Based on an initiation age of ~1.3 Ma and a total shortening of 740 ± 110 m [*Li et al.*, 2013], the Mushi fold has an average shortening rate of ~$0.6^{+0.1}/_{-0.1}$ mm/yr. The Atushi and Kashi folds in the Kashi-Atushi fold-and-thrust belt have shortened at an average rate of 2.25–2.75 mm/yr since their initiation ~1.2 and ~1.1 Ma, respectively, based on magnetostratigraphic dating of growth strata on the flanks of the anticlines [*Heermance et al.*, 2008]. The westernmost section of the Mutule fold has an average shortening rate of ~$2.0^{+1.1}/_{-0.6}$ mm/yr, from an estimated initiation age of 0.8 Ma and a shortening of 2.4 km [*Scharer et al.*, 2004]. Approximately 10 km east of the western fold tip, recent surface mapping and new, unpublished proprietary seismic data suggest that total shortening increases to ~6 ± 0.5 km and the initiation age was likely ~1.4 ± 0.7 Ma [*Bufe et al.*, 2017b], leading to an estimated Quaternary shortening rate of ~4 ± 2 mm/yr.

3. Late Quaternary Shortening in the Western Tarim Basin

As summarized below, late Quaternary shortening rates have been determined for eight structures in the western Tarim foreland [*Li*, 2012; *Li et al.*, 2012, 2013, 2015b; *Thompson*, 2013]. Sparse seismic activity, a weak InSAR signal, and low convergence rates from geodetic studies indicate a slow modern slip rate (<1 mm/yr) on the MPT on the northeastern Pamir margin (Figure 1b) [*Zubovich et al.*, 2010; *Li et al.*, 2012; *Bufe* et al., 2017a; *Qiao et al.*, 2017]. Slip rates along the westward continuation of the MPT are ~6 mm/yr during the Holocene [*Arrowsmith and Strecker*, 1999], although minimum shortening rates since the Miocene are much lower: 0.7–0.8 mm/yr [*Coutand et al.*, 2002]. Recent upper Quaternary scarps exist along the Kenenbierte and Takegai thrusts, but no geomorphic evidence indicative of recent or active slip has been observed along the MPT. Our field observations of older uplifted alluvial fans and a cosmogenic burial age of ~$2.2^{+4.4}/_{-1.3}$ Ma from growth strata related to the MPT, however, indicate that the fault was active during the Quaternary [*Thompson*, 2013; *Thompson et al.*, 2015].

In the Mayikake Basin, the Bieertuokuoyi Frontal Thrust (BFT) and the Mayikake Thrust (MT) cut a terrace that is dated to ~14.2 ka (Loc. 1, Figure 1) [*Thompson*, 2013]. The BFT, a segment of the PFT, places Paleogene marine rocks over Quaternary gravels [*Li et al.*, 2012]. Shortening rates along the BFT and MT (Figure 1) are ~4.6 and ~3.7 mm/yr, respectively [*Thompson*, 2013]. Across the Kezilesu River, the Jilegeyoute Thrust (JT) (Loc. 3, Figure 1) has a shortening rate of ~0.2 mm/yr [*Li*, 2012]. Farther east, where the PFT is exposed below the Tuomuluoan anticline (Loc. 1, Figure 1), magnetostratigraphy, field relationships, and a cosmogenic burial age constrain the shortening rate to >6.4 mm/yr [*Li et al.*, 2012; *Thompson*, 2013]. In addition, offset

features observed on recent satellite imagery analysis, integrated with geomorphic field work, have been interpreted as a suite of 2–3 en echelon active dextral faults (Loc. 8, F1; Figure 1) on the northeastern margin of the Pamir [*Fu et al.*, 2010]. Based on the offset geomorphic features, these faults have an estimated late Quaternary dextral slip rate of ~4.0 ±1.0 mm/yr [*Fu et al.*, 2010]. Furthermore, young folds within the Pamir-Tian Shan foreland also record late Quaternary deformation rates [*Scharer et al.*, 2006]. Deformed terraces crossing the Mushi anticline (Loc. 2, Figure 1) indicate that the fold is shortening at a rate of ~1.5 mm/yr since ~130 ka [*Li et al.*, 2013]. The Mingyaole anticline (Loc. 4 and Loc. 7, Figure 1), a detachment fold, is shortening at a rate of ≥5.0 mm/yr [*Thompson*, 2013; *Li et al.*, 2015b]. To the north of the Atushi anticline, the Atushi Thrust at the Boguzihe water gap (Loc. 5, F2; Figure 1) has a shortening rate of 3.5–6.0 mm/yr based on thermoluminescence (TL) dating [*Shen et al.*, 2001]. Here, these rates are considered preliminary estimates due both to perhaps unreliable TL ages, which appear too young given recent dating of nearby terraces at a similar level [*Bufe et al.*, 2017b] and to an inappropriate kinematic model, in which the shortening was calculated using a thrust-fault model but the measurements of the deformation were extracted from warped terraces. Finally, recent paleoseismic trenches on the Mingyaole South Thrust—a fault that ruptured in the 1985 M_w 7.4 Wuqia event (Loc. 6, Figure 1)—determined a slip rate of ~2 mm/yr and a recurrence interval of ~1.0 kyr [*Yang*, 2013]. Together, these data broadly agree with present-day GPS velocities across the region (Figure 1b) [*Mohadjer et al.*, 2010; *Ischuk et al.*, 2013; *Zubovich et al.*, 2016] and recent InSAR analyses [*Bufe et al.*, 2017a; *Qiao et al.*, 2017] and provide a foundation to create a robust spatial and temporal framework for interpreting the deformation rates, Quaternary history, and spatial patterns in the western Tarim Basin.

4. Methods

Fluvial terraces can serve as passive strain markers, recording the amount of deformation that occurred since terrace abandonment: deformation that can be used to constrain recent rates of horizontal shortening [e.g., *Rockwell et al.*, 1984; *Lave and Avouac*, 2000; *Thompson et al.*, 2002]. We quantified the deformation recorded by well-preserved fluvial terraces that cross active structures using differential GPS (dGPS) surveys and optically stimulated luminescence (OSL) dating of the terrace surfaces. Where possible, we mapped the underlying bedrock to determine the kinematic pathway of deformation in order to calculate shortening rates more accurately.

Our dGPS surveys were collected using a high-precision, real-time kinematic GPS system to quantify the amount of deformation on each terrace surface and the riverbed. The data were postprocessed relative to a base station, yielding elevations with ~40 cm vertical accuracy. Where we were unable to collect dGPS data or it was later realized that the dGPS data did not span the entire structure, elevations were extracted perpendicular to the structure, and parallel to the dGPS surveys, from the 90 m Shuttle Radar Topography Mission digital elevation model (SRTM DEM) [*Farr et al.*, 2007]. At Kangxiwar, terraces situated on the side of an eroding cliff face prohibited us from surveying the actual terrace surface. Instead, we used a combination of dGPS surveys and laser-range measurements to determine the strath terrace gradient. For each terrace, we assumed the original terrace gradient approximated the modern channel gradient, such that we surveyed and subtracted the modern channel to define the recent deformation of the terraces. Least squares linear regression was used to fit lines through each terrace tread, whose offset since deposition was then calculated at the midpoint on the folded limb. Uncertainties in the offset, total slip, and the slip rate were simulated using a Monte Carlo approach [e.g., *Thompson et al.*, 2002; *Li et al.*, 2012; *Goode et al.*, 2014]. Errors in slip and shortening rates are reported with 95% confidence intervals around the modal rate.

After mapping the terrace surfaces and recording bedding and fault dips underlying the deformed surfaces, we classified each structure into one of five simple kinematic models in order to calculate the slip and shortening magnitudes. We classified structures as a fault-bend fold [*Suppe*, 1983; *Chen et al.*, 2007b], detachment fold [*Poblet and McClay*, 1996; *Li et al.*, 2015b], thrust fault, listric thrust fault [*Amos et al.*, 2007], or an undetermined structure (Figure 3). For fault-bend folds and detachment folds, we followed *Chen et al.* [2007b] and *Li et al.* [2015b], respectively, to calculate magnitudes and rates of slip and shortening (Figures 3a and 3b). Slip and shortening for thrust faults followed conventional methods (Figure 3c), whereas calculations for listric thrust faults followed *Amos et al.* [2007] (Figure 3d). For sites where we could not clearly define a structural style, we classified these structures as undetermined and applied simple line-length
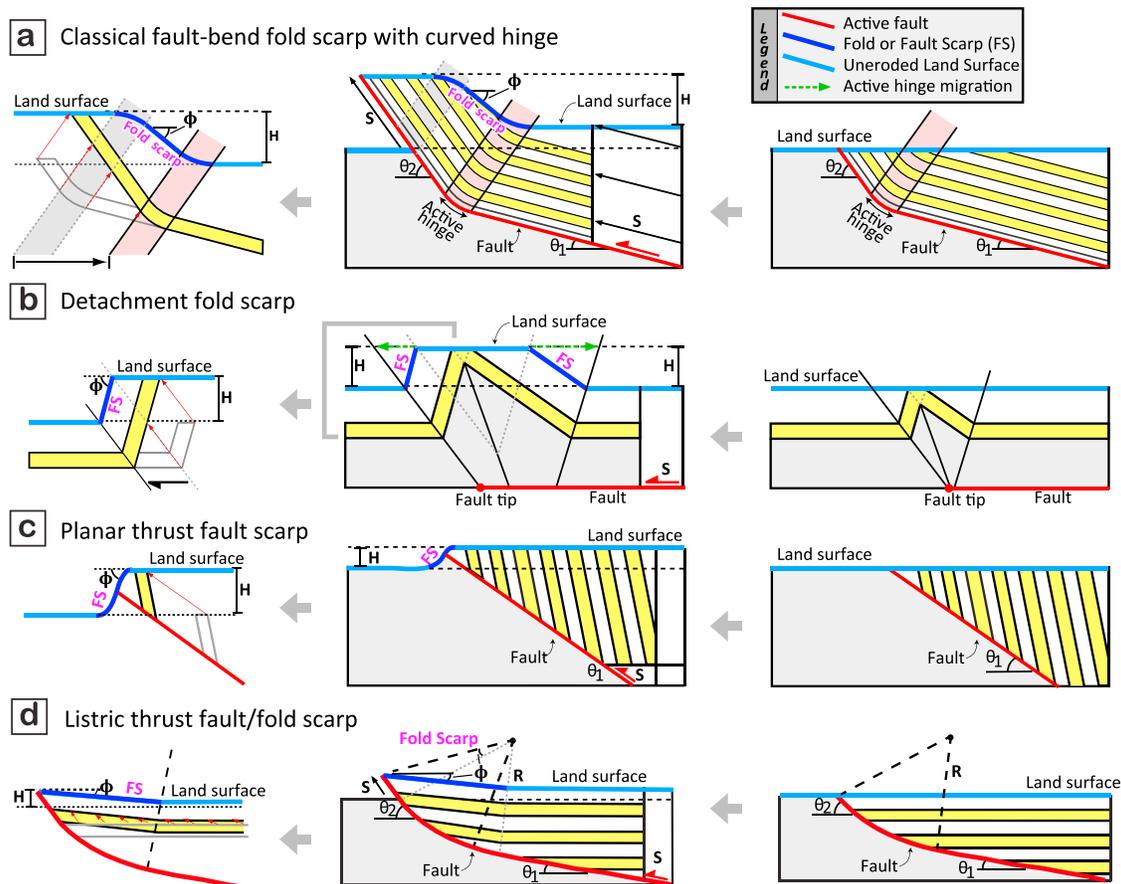
Figure 3. Kinematic models of active fold and fault scarps used to calculate slip and shortening rates and magnitudes in this study. H: fold or fault scarp height; ϕ: fold scarp or backtilted terrace slope; θ_1 and θ_2: fault dips; S: fault slip increment; R: radius of curvature. (a) Classical fault-bend fold scarp with a curved hinge, formed from differential uplift across an active hinge pinned to a fault at depth. The bed and land surface movement can be described by a set of hinge-parallel slip vectors (thin red arrows). Modified from *Yue et al.* [2011] and *Li et al.* [2015b]. (b) Detachment fold scarp, formed from the migration of hinges that are pinned to a detachment surface. Modified from *Poblet and McClay* [1996] and *Li et al.* [2015b]. The bed and land surface movement can be described by a set of hinge-parallel slip vectors. (c) Thrust fault scarp, formed from slip along a planar fault that cuts the terrace surface. The bed and land surface movement can be described by a set of fault-parallel slip vectors. (d) Listric thrust fault scarp, formed from movement along a listric thrust that is rooted at depth into a planar ramp. Rotation over the listric thrust leads to tilting of the backlimb that is proportional to the total amount of slip on the underlying thrust fault. Modified from *Amos et al.* [2007]. The bed and land surface movement can be described by a set of progressively rotating slip vectors, which are parallel to the planar fault at depth but gradually rotate to become parallel to the curved fault dip at the surface.

unfolding to approximate the shortening, while recognizing these types of structures have larger uncertainties associated with their results. Trishear models [*Erslev*, 1991; *Vázquez et al.*, 2016] were not tested because field observations suggest most folds can be described by kink-band geometries with well-defined hinge zones and exposure of the studied faults are a simple planar fault plane with no evidence of a triangular tip zone.

To date each deformed surface, we collected fine-grained quartz OSL samples from weakly consolidated, fluvial sediments. These samples date the time of sediment deposition, commonly above a strath surface, which we assume approximates the timing of terrace abandonment. The OSL samples were processed in the Laboratory of Luminescence Research at the Institute of Geology at the China Earthquake Administration in Beijing, China, following the sensitivity-corrected, multiple aliquot, regenerative dose protocol for silt-sized (4–11 μm) quartz [*Lu et al.*, 2007] (Tables 1 and 2). Elemental concentrations of U, Th, Rb, and K for dose rates were measured at the ALS Minerals Lab in Reno, NV, or using a thick-source alpha counting technique (for U and Th only) and X-ray fluorescence (for K) at the China Earthquake Administration

Table 1. OSL Sample Descriptions

Sample No.	Latitude/Longitude	Terrace Level	Depth (m)	Thickness of Sampled Deposit (cm)	Lithology
Bieertuokuoyi Fold Scarp Terraces					
LED10-213	39.5054°N/75.0260°E	T4	5.0	5	muddy silt
LED10-219	39.5054°N/75.0260°E	T4	5.0	5	muddy silt
LED11-347	39.5052°N/75.0271°E	T4	3.5	15	silty fine sand
LED11-348	39.5052°N/75.0271°E	T4	2.5	30	muddy silt
LED11-308	39.5059°N/75.0130°E	T2	4.0	15	silt
LED11-349	39.5059°N/75.0130°E	T2	4.0	15	silt
Bieertuokuoyi Fan					
LED11-350	39.3918°N/74.9944°E		4.5	5	silty fine sand
LED11-307	39.3849°N/75.0017°E		50	5	silt
Aismaola Fold Scarp Terraces					
LED11-352	39.3433°N/75.4210°E	T2	1.0	8	laminated silt
LED11-306	39.3473°N/75.4170°E	T3	1.5	5	silt
Kangsu Fault Scarp Terrace					
LED10-331	39.6159°N/75.0357°E	T2	10	20	laminated fine sand
LED10-332	39.6159°N/75.0357°E	T2	10	20	laminated fine sand
Kangxiwar Fold Scarp Terrace					
LED11-354	39.6725°N/75.3716°E	T1	16	8	fine sand silt
LED10-330	39.3672°N/75.0017°E	T1	31	31	fine sand
Wuheshalu Fold Scarp Terrace					
LED10-218	39.7775°N/74.7405°E	T2	25	6	silt

Table 2. OSL Dating Results

Sample No.	Bulk Alpha (ks^{-1} cm^{-2})	U (ppm)	Th (ppm)	K (%)	Rb (ppm)	Saturated Water Content (%)	Water Content (%)	Dose Rate (Gy/ka)	Equivalent Dose (Gy)	Age (ka)
Bieertuokuoyi Fold Scarp Terraces										
LED10-213	11.3 ± 0.2	-	-	1.97	-	46	23 ± 23	3.6 ± 0.2[a]	309.1 ± 15.6	85.0 ± 18.9
LED10-219	11.4 ± 0.2	-	-	2.11	-	46	23 ± 23	3.7 ± 0.2[a]	256.6 ± 22.9	71.5 ± 14.4
LED11-347	5.2 ± 0.1	-	-	1.09	-	23	11 ± 11	2.1 ± 0.1[a]	232.8 ± 9.9	109.7 ± 6.7
LED11-348	9.9 ± 0.2	2.6	9.7	1.77	87.7	33	16 ± 16	3.5 ± 0.2[a]	250.5 ± 26.0	68.1 ± 17.4
								mean age		**97.9 ± 5.5**
LED11-308	5.4 ± 0.1	-	-	1.38	-	23	11 ± 11	2.4 ± 0.1[a]	288.0 ± 18.6	120.1 ± 11.5
LED11-349	8.4 ± 0.2	-	-	1.48	-	36	18 ± 18	2.8 ± 0.1[a]	276.3 ± 24.6	97.7 ± 13.1
Bieertuokuoyi Fan										
LED11-350	-	1.4	4.9	1.04	43.4	19	9 ± 9	2.3 ± 0.2[b]	198.6 ± 20.4	88.0 ± 11.2
LED11-307	6.3 ± 0.1	-	-	1.48	-	33	16 ± 16	2.4 ± 0.1[a]	207.5 ± 16.1	87.1 ± 11.0
								mean age		**87.5 ± 8.3**
Aismaola Fold Scarp Terraces										
LED11-352	-	2.8	9.8	1.72	81.9	29	14 ± 14	3.9 ± 0.5[b]	210.5 ± 11.5	54.2 ± 8.1
LED11-306	9.1 ± 0.2	-	-	1.76	-	42	21 ± 21	3.1 ± 0.2[a]	294.3 ± 15.5	96.1 ± 11.9
Kangsu Fault Scarp Terrace										
LED10-331	9.1 ± 0.2	-	-	2.14	-	45	22 ± 22	3.3 ± 0.6[a]	371.5 ± 46.2	111 ± 22
LED10-332	-	1.7	9.6	1.98	91.1	45	22 ± 22	3.3 ± 0.7[b]	414.5 ± 46.2	127 ± 15
								mean age		**122 ± 13**
Kangxiwar Fold Scarp Terrace										
LED11-354	-	1.5	5.3	0.96	50.6	16	8 ± 8	2.2 ± 0.2[b]	223.7 ± 11.5	101.2 ± 10.6
LED10-330	-	2.9	11.5	2.24	116	25	12 ± 12	4.5 ± 0.6[b]	255.3 ± 19.2	56.9 ± 8
								mean age		**56.9 ± 8[c]**
Wuheshalu Fold Scarp Terrace										
LED10-218	9.5 ± 0.4	-	-	1.91	-	42	21 ± 21	3.3 ± 0.4[a]	134.5 ± 25.4	41.3 ± 13.4

[a]Fine-grain dose rate, calculated using bulk alpha and K.
[b]Fine-grain dose rate, calculated using U, Th, K, and Rb (1σ uncertainty).
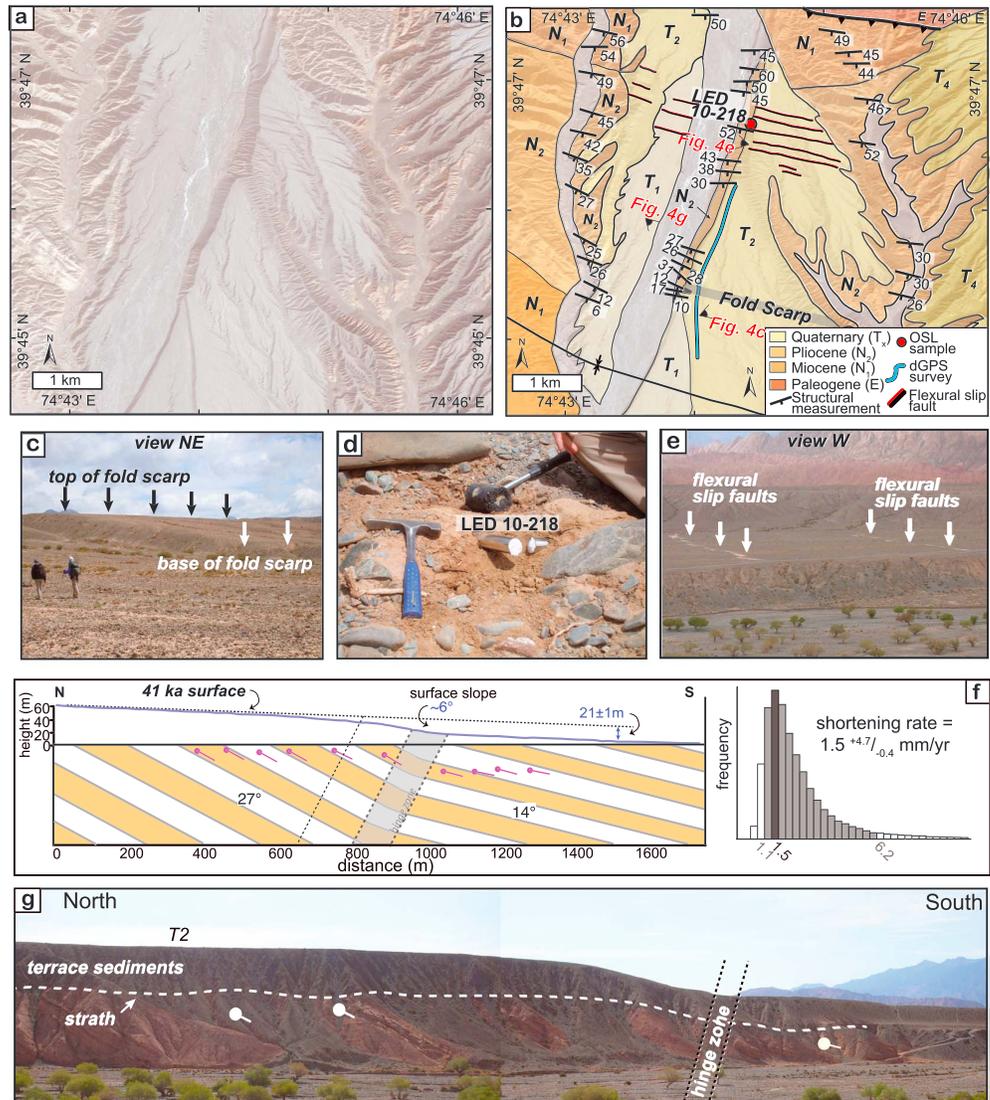[c]Mean age does not include sample LED11-354. See text.

Figure 4. (a) Google Earth image and (b) geomorphic map of the Wuheshalu fold scarp. (c) Field photo of the folded T2 terrace. Location in Figure 4b. (d) Photo of sample LED10–218. Location in Figure 4b. (e) Photo of the flexural slip fault scarps on the T1 terrace, which are <70 cm high [*Li et al.*, 2017]. Location in Figure 4b. (f) dGPS survey of T2 terrace surface and shortening rate. (g) Photo of the folded T2 terrace. Location in Figure 4b.

(Table 2). Additional details on the OSL sample collection and processing can be found in the supporting information. All OSL ages are reported with 1σ uncertainty unless otherwise stated.

5. Shortening Rates Along the Southern Tian Shan

5.1. Wuheshalu Fold Scarps

Along the Wuheshalu River Valley, three flights of gravel-covered strath surfaces that lie 35–65 m above the modern river level have been beveled into Neogene bedrock and are deformed near the core of a large syncline on the southern front of the Tian Shan (Figures 4a and 4b). The dips of the underlying bedrock change from 27° to 14° down the length of the river valley, with the measurements defining two dip panels clearly separated by a hinge zone that is ~90 m wide (Figure 4f).

Table 3. Summary of Deformed Surfaces, Corresponding Structures, and Parameters Used to Calculate Shortening and Shortening Rate

Deformed Surface	Structure	Type of Structure[a]	Dips Related to Structure		Scarp Height (m)[c]	Scarp Length (m)[d]	Total Shortening (m)[c]
			$\theta_1(°)$[b]	$\theta_2(°)$[b]			
Bieertuokuoyi South Fan	Kenenbierte Thrust	Undefined	-	-	-	-	≥19.8
Bieertuokuoyi fold scarp T4	Pamir Frontal Thrust/Bieertuokuoyi segment	Fault bend fold	50	62	70	720	540
Bieertuokuoyi fold scarp T3	Pamir Frontal Thrust/Bieertuokuoyi segment	Fault bend fold	50	62	63	480	370
Bieertuokuoyi fold scarp T2	Pamir Frontal Thrust/Bieertuokuoyi segment	Fault bend fold	50	62	9	330	48
Aismaola fold scarp T2	Pamir Frontal Thrust/Aismaola segment	Fault bend fold	36	60	>12	>555	>44
Aismaola fold scarp T3	Pamir Frontal Thrust/Aismaola segment	Fault bend fold	36	60	>15	>230	>55
Wuheshalu fold scarp	Wuheshalu syncline	Fault bend fold	14	27	21	150	48
Kangsu fault scarp	Kangsu South Thrust	Thrust fault	45	-	5	-	7
Kangsu West fault scarp 1	Kangsu West Fault Zone	Thrust fault	30	-	3.5	-	9
Kangsu West fault scarp 2	Kangsu West Fault Zone	Oblique thrust fault	40	-	14.5[e]	-	21
Kangsu West fault scarp 3	Kangsu West Fault Zone	Thrust fault	40	-	14.8[f]	-	16
Kangxiwar	Atushi Fault	Listric thrust fault	30	57	>44	>915	86

[a]Refer to Figure 3 for kinematic models of different structures.
[b]Bedding dips measured in field. See Figure 3 for locations of θ_1 and θ_2 on structure. Modeled with uncertainty of ±5°, except for Wuheshalu, where uncertainty was ±3°.
[c]Scarp height and total shortening are modal outputs from Monte Carlo model based on differential GPS topographic survey of terrace surface and age. See text for additional details.
[d]Scarp length (preserved) for fold scarps and the backlimb of the listric thrust model calculated from differential GPS topographic surveys.
[e]Fault also has a strike-slip component, with ~45 m of lateral offset.
[f]Fault also has a strike-slip component, with ~32 m of lateral offset. Total offset includes vertical offset from both fault scarps (11.3 m + 3.5 m from p5 and p4, respectively).

We surveyed a deformed terrace, T2, that is well preserved across the axial hinge. Above the T2 strath, the terrace cover is as thick as ~30 m and is primarily cobble-boulder conglomerate with well-rounded clasts, uncommon sand and silt lenses, and a moderately well-developed desert pavement. Flexural-slip scarps cut across all the terraces and are clearly visible in the field as linear features of silt that line up with the bedding (Figure 4e) [*Li et al.*, 2017]. On the T2 surface, the flexural slip scarps are <4.3 m high, whereas on the lower T1 surface, they are <70 cm high [*Li et al.*, 2017]. The T2 terrace surface has a slope of ~6°, and a scarp height and length of ~21 m and ~150 m (Table 3), respectively. We calculated the shortening based on a fault-bend fold model [*Chen et al.*, 2007b] because the syncline may be caused by a south dipping fault to the north of the fold scarps [*Xue et al.*, 2014]. We note that because this structure is not clearly fault related, we can also model the shortening using the equations in *Li et al.* [2015b], which rely solely on the dip of the underlying bedrock and the hinge width, independent of any related faults. Based on the fold scarp model following *Chen et al.* [2007b], the total shortening is ~48 m (Table 3), whereas the fold scarp model of *Li et al.* [2015b] yields an incremental shortening of 7.8 m. One reason for the large discrepancy is that different kinematic models were applied: the classical fault-bend fold scarp model determines shortening for the entire fold assuming deformation is caused by the fault at depth, whereas the migrating hinge model of *Li et al.* [2015b] only calculates the incremental shortening recorded by that particular terrace and hinge assuming a detachment-fold geometry. Thus, the incremental shortening should be viewed as a minimum shortening across the structure, given that other migrating axial hinges may exist and record deformation [e.g., *Li et al.*, 2015b].

A single, fine-grain OSL sample (Figure 4d), collected from a ~ 6-cm-thick silt lens 25 m below the surface, dates the T2 surface to 41.3 ± 13.4 ka (Tables 1 and 2). This age yields a total shortening rate of the Wuheshalu fold scarp of 1.5 $^{+4.7}/_{-0.4}$ mm/yr following the fault-bend fold model. The incremental shortening rate following the migrating-hinge fold scarp model of *Li et al.* [2015b] is ~0.2 mm/yr.

5.2. Kangsu Fault Scarps
5.2.1. Kangsu South Thrust
The Kangsu South Thrust, a thick-skinned fault of the southern Tian Shan, places Cretaceous and Jurassic strata over the Pliocene Atushi Formation. The fault is exposed in the Kangsu River Valley (Figures 1, 5a, and 5b), and farther south, Precambrian metamorphic rocks are uplifted in the hanging wall of the fault along the Kezilesu River (Figure 1) [*Wang et al.*, 2016]. The fault dips ~45° to the north, exposes an ~1-cm-thick
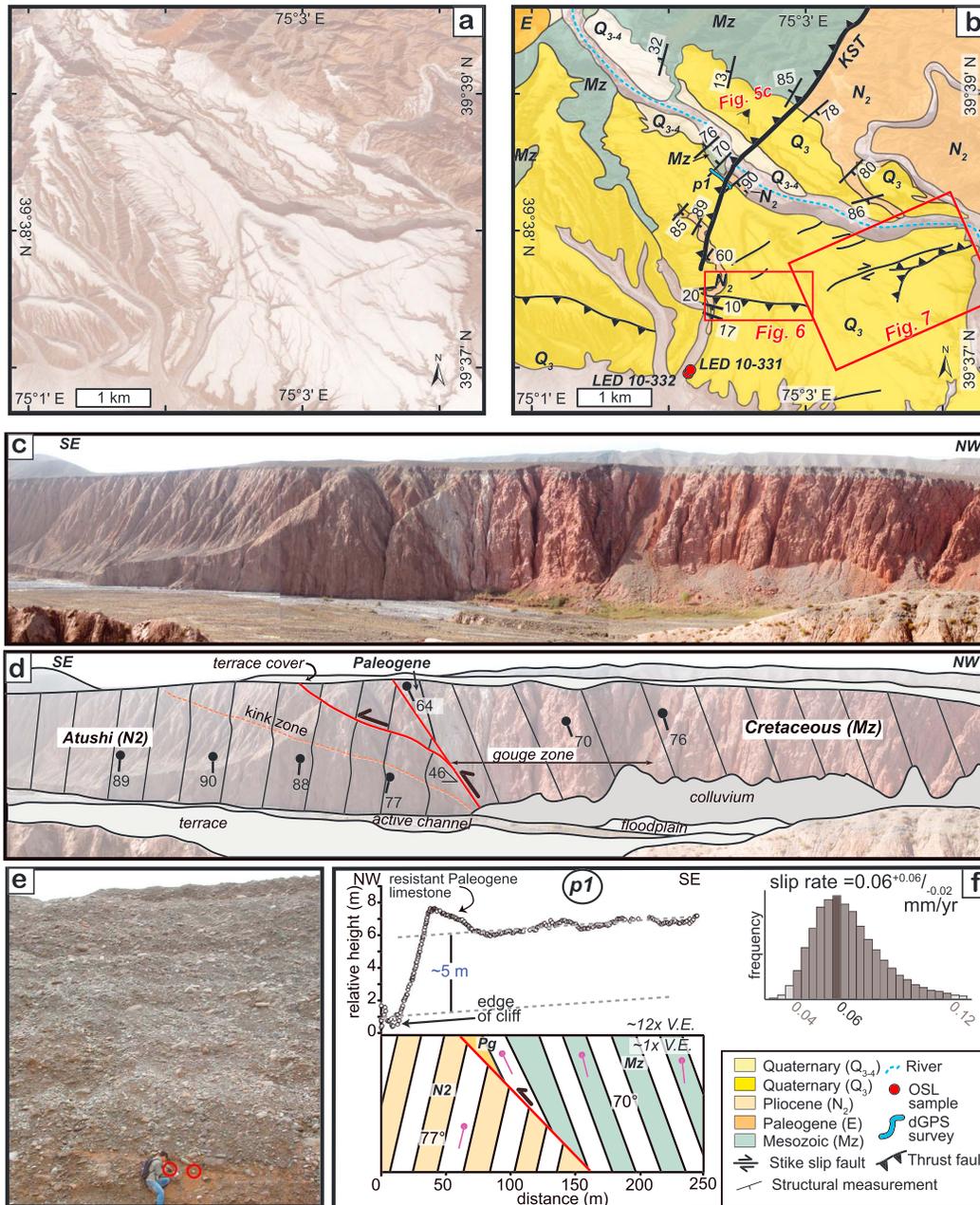
Figure 5. (a) Google Earth image and (b) geomorphic map of the Kangsu South Thrust Fault Scarp. (c) Photo and (d) annotated photo of the fault scarp. Location in Figure 5b. (e) Photo of Kangsu terrace fill and OSL samples LED 10-331 and LED 10-332, marked by red circles. Location in Figure 5b. (f) dGPS survey profile p1 and slip (equal to shortening, based on a fault that flattens at depth, see text) rate.

calcite layer along the fault itself, and has a thick (~100 m) gouge zone, extending into both the hanging wall and footwall stratigraphy (Figures 5c and 5d).

A terrace surface currently lies ~90 m above the modern Kangsu riverbed. A thin terrace cover of ~2 m rests on top of the beveled strath near the fault scarp. Farther downstream, toward the confluence with the Kezilesu River, the bouldery terrace cover is ~55 m thick, suggesting differential uplift/erosion of the bedrock from the Kangsu River and Kezilesu River. The terrace fill is composed of cobble and boulder gravels with very
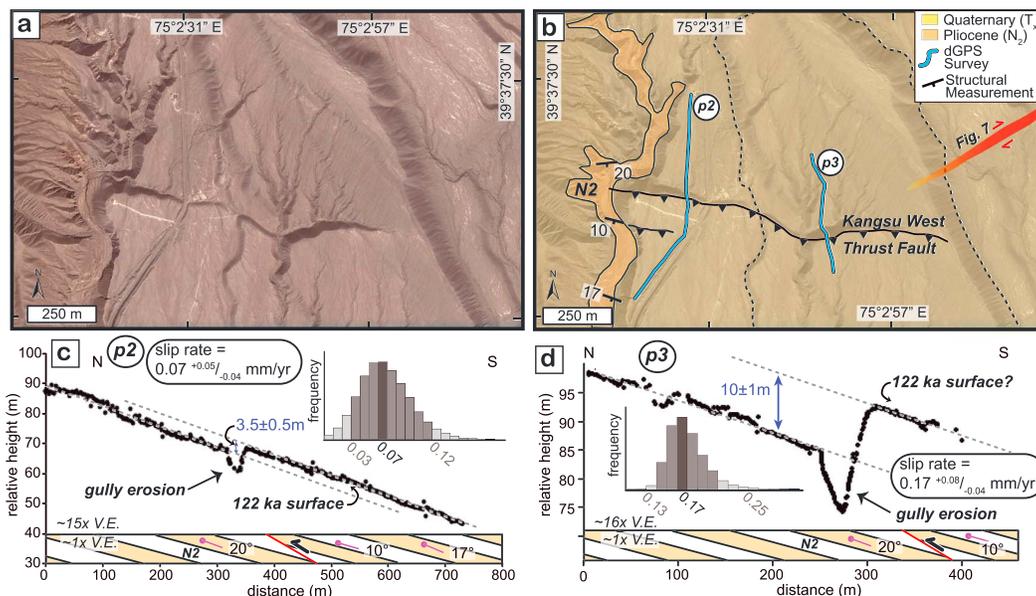
Figure 6. (a) Google Earth image and (b) geomorphic map of the Kangsu West Fault Scarp. (c) p2 dGPS survey of the terrace and slip rate. (d) p3 dGPS survey of the terrace and slip rate.

uncommon silt or sand lenses. The surface has a moderately developed desert pavement with varnished clasts that are heavily fractured. Although the KST is the major fault cutting this surface, several south vergent faults and north vergent flexural slip faults offset the surface farther south (Figures 5a, 5b, 6, and Figure 7).

DGPS surveys indicate that the KST displaces the highest terrace surface by 5–7 m. Complicating the interpretation, the fault scarp coincides with a relict terrace riser, and thus, some of the observed offset may be due to geomorphic processes instead of subsequent faulting. Using a conservative estimate of 5 m of vertical offset by the fault and the observed fault dip of 45°, the terrace records ~7.1 m of slip (Table 3). Younger terraces on the eastern side of the river (Q3-Q4, Figure 5a) do not record any deformation by this fault.

Two OSL samples were collected from ~20-cm-thick fine sand lenses in gravel of the highest river terrace approximately 10 m below the terrace surface. The resultant OSL ages agree with each other within error, yielding ages of 111 ± 22 and 127 ± 15 ka, and a weighted mean depositional age of 122 ± 13 ka (Tables 1 and 2). Using an estimated slip of ~7.1 m, the slip rate on this strand of the KST since 122 ± 13 ka is ~0.1 mm/yr (Figure 5f). Based on unpublished, proprietary seismic lines, this fault flattens at depth, and thus, the slip rate can be approximated as a shortening rate. Despite the low rate on the KST, numerous other fault scarps in the Kangsu West Thrust Fault Zone, described below, cut the Quaternary terrace, suggesting that the strain may be more distributed across this area in recent times (Figure 5b).

5.2.2. Kangsu West Thrust Fault Zone

Farther south on the same terrace, a south-dipping thrust fault offsets the terrace, cutting the underlying Pliocene Atushi Formation (Figures 6a and 6b). The fault strikes approximately east-west, dips 30°S, and is exposed in the riverbed to the west of the fault scarp. We collected two surveys across the fault scarp, which reveal vertical offsets between 4 and 10 m. On profile 2 (p2) (Figure 6c), the terrace is vertically offset ~3.5 m, and the slip is ~7 m, using a fault dip of 30° and following model C for a simple thrust fault (Table 3 and Figure 3). The slip rate on this fault since 122 ± 13 ka is ~0.1 mm/yr (Table 4). On profile 3 (p3) (Figure 6d), the terrace is offset ~10 m, and the total slip is 20.4 m (Table 3). The slip rate since 122 ± 13 ka is ~0.2 mm/yr. Thus, we estimate this fault has a shortening rate of ~0.1–0.2 mm/yr. The varying offset along the fault may have several explanations: (1) the fault scarp has been partially eroded by the gullies forming in front of the fault scarp (Figures 6c and 6d); (2) differential offset occurs along the fault, with strain being distributed on several smaller, unstudied faults on the terrace surface that did not cross our
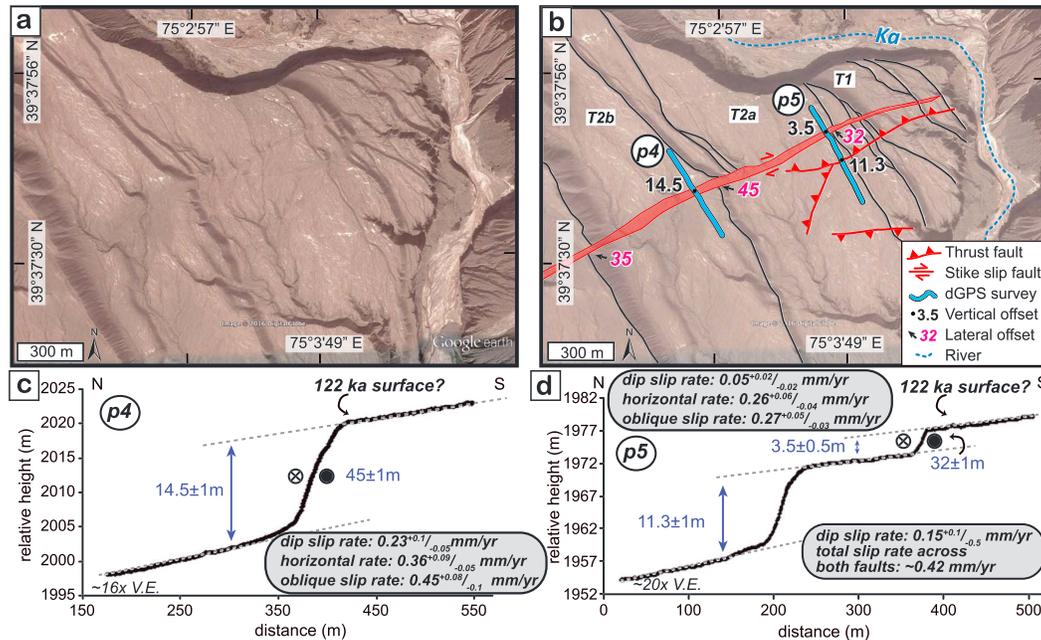
Figure 7. (a) Google Earth image and (b) geomorphic map of the Kangsu West Fault Zone, with a dextral oblique thrust and a south vergent thrust. (c) dGPS survey p4 of the terrace and slip rates crossing only the oblique thrust fault. (d) dGPS survey p5 of the terrace and slip rates crossing both faults. Ka = Kangsu River.

dGPS surveys (Figure 6b); and (3) the fault cuts terraces of different ages. In fact, p3 may have been measured on a slightly older terrace (outlined in dashed black line, Figure 6b). In this case, using an age of 122 ± 13 ka would provide a minimum age for the surface and a maximum slip rate.

A few hundred meters to the east, two thrust faults, one of them a right-lateral oblique thrust, cut the terrace surface (Figures 7a and 7b). Geomorphic mapping suggests that this faulted terrace is the same broader terrace surface, with an age of 122 ± 13 ka. Both faults strike approximately east-west and dip to the north, creating south-facing fault scarps. A shorter, smaller, north-facing fault scarp created by a south-dipping fault is present ~400 m to the south and was not surveyed. Only the southern thrust fault, dipping 40°N, crops out. Profile 4 (p4) crosses only the oblique thrust fault (Figure 7c). The terrace is vertically offset by ~14.5 m, and assuming a similar 40° fault dip, records ~21 m of vertical slip and a dip-slip rate of ~0.2 mm/yr (Table 3). The terrace riser adjacent to p4 is dextrally offset by ~45 m (Figure 7b), suggesting a lateral slip rate of ~0.4 mm/yr. Together, p4 records an oblique slip rate of ~0.5 mm/yr since 122 ± 13 ka. Profile 5 (p5) crosses both the oblique slip and the thrust fault (Figure 7d). The southern thrust fault offsets the terrace surface ~11.3 m, and records ~16 m of slip along the fault, yielding a dip slip rate of ~0.2 mm/yr (Table 3). Profile p5 also records ~3.5 and ~32 m of vertical and dextral offset on the oblique slip thrust and 5.5 m of vertical slip. These offsets result in a dip slip rate of ~0.1 mm/yr and a lateral slip rate of ~0.3 mm/yr that, together, suggest an oblique slip rate of ~0.3 mm/yr. Combined with the slip on the thrust fault, these two faults record ~0.4 mm/yr of deformation, similar to the slip recorded along profile p4 (Figure 7c). Although the slip is distributed on two faults, the fault zone has a total dextral oblique slip rate of ~0.4–0.5 mm/yr. Parallel to the orogenic convergence direction, however, the northward shortening rate on the Kangsu West Fault Zone is ~0.2 mm/yr, with slip distributed across up to three faults that strike approximately east-west (Table 4 and Figures 6 and 7).

5.3. Backtilted Kangxiwar Terraces

In the hanging wall of the Atushi Fault, nearly flat-lying siltstones and sandstones, interbedded with pebble conglomerates, rest above a strath surface beveled into the Miocene Wuqia Group (N1) (Figures 8a and 8b). The terrace fill is discontinuous with a variable thickness between 10 and 40 m created by ongoing rapid erosion. Presently, the strath terrace surface lies ~30 m above the modern riverbed and gently slopes 3° to

Table 4. Summary of Quaternary Shortening Rates in the Western Tarim Basin

Deformed Surface	Structure	Age (ka)	Rate (mm/yr)	References
Western Structures				
Since 2.6 Ma				
	Pamir Frontal Thrust	5000–6000[a]	10–12	*Chen et al.* [2010], *Thompson et al.* [2015], and *Cheng et al.* [2016]
	Shortening rate since 2.6 Ma:		**10–12**	
Since ~ 120 ka				
Bieertuokuoyi South Fan	Kenenbierte Thrust	~87[b]	$0.2^{+0.1}/_{-0.1}$	This study
Bieertuokuoyi fold scarp T4	Pamir Frontal Thrust/ Bieertuokuoyi segment	~98[b]	~5.6	This study
Kangsu fault scarp T2	Kangsu South Thrust	~122[b]	~0.1	This study
Kangsu West fault zone T2		~122[b]	~0.2	This study
Wuheshalu fold scarp T2	Wuheshalu syncline	~41[b]	$1.5^{+4.7}/_{-0.4}$	This study
	Shortening rate since 120 ka:		$\mathbf{7.6^{+4.8}/_{-0.6}}$	
Since ~ 15 ka				
Bieertuokuoyi Frontal Thrust	Pamir Frontal Thrust/ Bieertuokuoyi segment	~14[c]	~4.6	*Thompson* [2013]
Mayikake Thrust	Pamir Frontal Thrust	~14[c]	~3.7	*Thompson* [2013]
Jilegeyoute Thrust	Jilegeyoute Thrust	~14[b]	~0.2	*Li* [2012]
	Shortening rate since 15 ka:		**8.5**	
Eastern Structures				
Since 2.6 Ma				
	Kashi anticline	~1100[d]	2.25–2.75	*Heermance et al.* [2008]
	Atushi anticline	~1400[d]	2.25–2.75	*Heermance et al.* [2008]
	Mutule anticline	~800[e]	$2.0^{+1.1}/_{-0.6}$	*Scharer et al.* [2004]
	Mingyaole anticline	~1600[a]	1.1–1.9	*Chen et al.* [2005] and *Li et al.* [2015b]
	Mushi anticline	~1300[f]	$0.6^{+0.1}/_{-0.1}$	*Li et al.* [2013] and *Thompson* [2013]
	Shortening rate since 2.6 Ma:		$\mathbf{9.1^{+2.5}/_{-1.5}}$	
Since ~ 0.35 Ma				
Pamir Frontal Thrust	Pamir Frontal Thrust	350[a]	>6.4	*Li et al.* [2012]
Since ~ 130 ka				
Aismaola anticline T3	Pamir Frontal Thrust/Aismaola segment	~96[b]	$>0.5^{+1.1}/_{-0.2}$	This study
Mushi anticline T4	Mushi anticline	~133[b]	$1.5^{+1.3}/_{-0.5}$	*Li et al.* [2013]
Atushi T4	Atushi anticline	~82[c]	~0.1	*Bufe et al.* [2017b]
	Shortening rate since 0.35 Ma:		$\mathbf{>8.5^{+2.4}/_{-0.7}}$	
Since ~ 55 ka				
Aismaola anticline T2	Pamir Frontal Thrust/Aismaola segment	~55[b]	$>0.7^{+1.3}/_{-0.2}$	This study
Mushi anticline	Mushi anticline	~55[b]	$1.5^{+1.3}/_{-0.5}$	*Li et al.* [2013]
Kangxiwar fold scarp	Atushi fault	~57[b]	$1.5^{+0.5}/_{-0.3}$	This study
Kashi anticline T4	Kashi anticline	~48[b]	2–3.4	*Bufe et al.* [2017b]
	Shortening rate since 55 ka:		$\mathbf{>6.4^{+3.8}/_{-1.7}}$	
Since ~ 15 ka				
Mingyaole anticline	Mingyaole anticline	~15[c]	>5	*Thompson* [2013] and *Li et al.* [2015b]
Mushi anticline	Mushi anticline	~15[b]	$1.5^{+1.3}/_{-0.5}$	*Li et al.* [2013]
Mutule anticline T1	Mutule anticline	~11[b]	1.4–2.4	*Bufe et al.* [2017b]
Mingyaole South Thrust	Mingyaole South Thrust	~6[b]	~2	*Yang* [2013]
	Shortening rate since 15 ka:		$\mathbf{>10.4^{+1.8}/_{-1.0}}$	

[a]Age determined using magnetostratigraphy and cosmogenic burial dating.
[b]Age determined using OSL.
[c]Age determined using ^{10}Be cosmogenic depth profile dating.
[d]Age determined using magnetostratigraphy.
[e]Estimated age. Farther east on Mutule, initiation age estimated to ~1.4 ± 0.7 Ma, with shortening rate of 4 ± 2 mm/yr [*Bufe et al.*, 2017b].
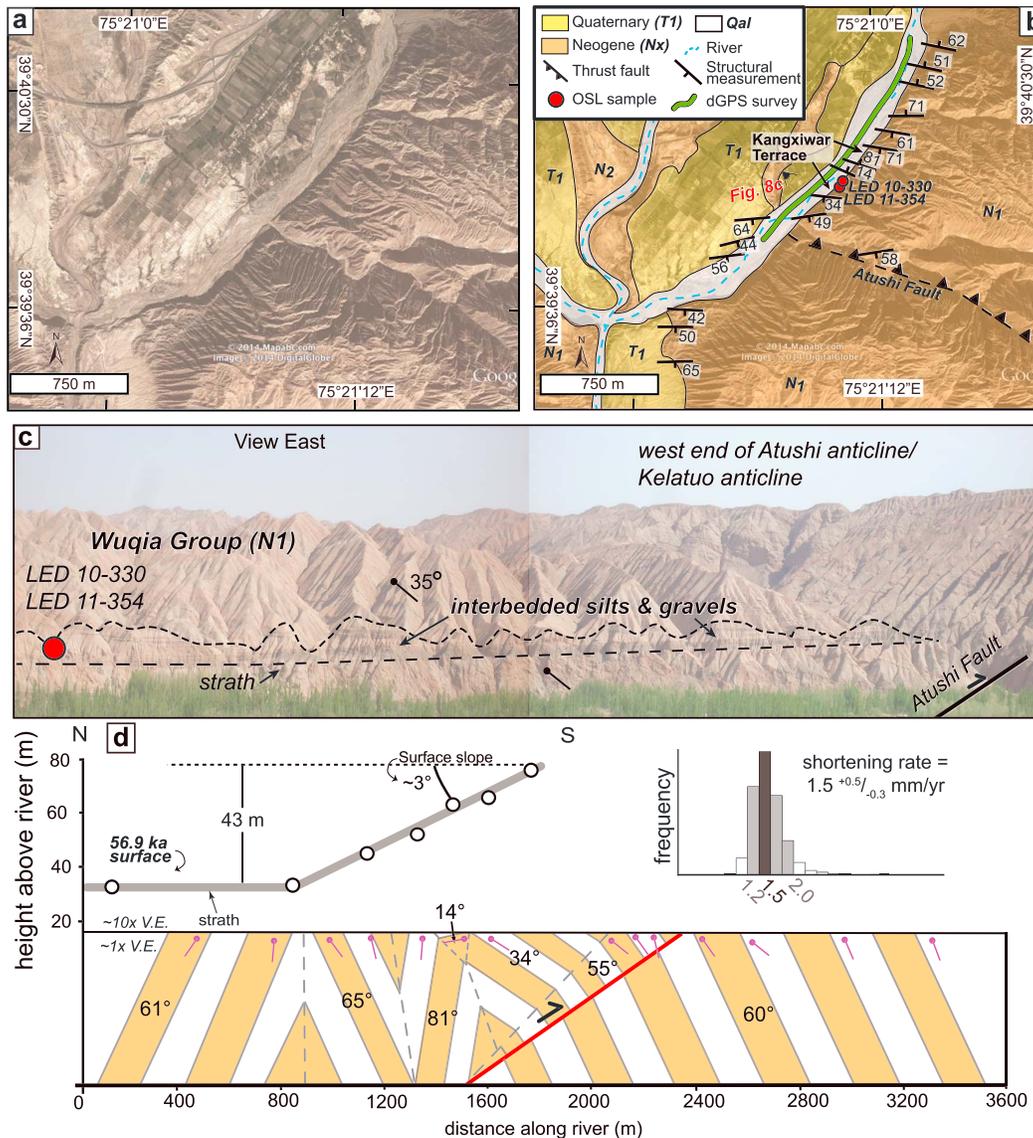[f]Age determined using cosmogenic burial dating.

Figure 8. (a) GoogleEarth image and (b) geomorphic map of the Kangxiwar fold scarp. (c) Photo of the subtle backtilted Kangxiwar terrace. The location of the Atushi Fault is approximate. Note the variable preserved thickness of terrace fill above the strath surface. OSL sample locations marked by red circle. The western end of the Atushi anticline is also referred to as the Kelatuo anticline (Figure 1, see text). Location of photo in Figure 8b. (d) dGPS survey of the terrace with underlying Neogene structure, and minimum shortening rate.

the north (opposite to the river's flow direction) with an increasing height above the river toward the Kelatuo/Atushi anticline and Atushi Fault (Figure 8d). The preserved backtilted surface is >915 m long (Table 3). The location on the side of a steep cliff prevented us from surveying and mapping the spatial extent of the deposits in detail. We acknowledge that the surface's apparent backtilt could reflect the depositional dip of an alluvial fan built by a north-flowing river. However, limited field observations of poorly imbricated cobble clasts in the terrace fill indicate a south-flowing river likely deposited the sediments.

We mapped the exposed Miocene bedding (Figure 8b) and relied on previous interpretations of the Atushi Fault and anticline from *Heermance et al.* [2008] to characterize the structure (Figure 2c). The Atushi anticline is commonly described as a detachment fold that initiated 1.2–1.4 Ma [*Scharer et al.*, 2004; *Chen et al.*, 2005; *Heermance et al.*, 2008], with a detachment surface at a depth between 4 and 6 km in the Miocene Wuqia

Group [*Heermance et al.*, 2008; *Fu et al.*, 2010]. Approximately ~15 km to the east of the Kangxiwar terrace, the Atushi anticline may be more similar to a fault-bend fold, and the Atushi Fault cuts the westward extension of the Atushi anticline, called the Kelatuo anticline, translating the anticline south above a 20–35° dipping convex-up fault (Figure 2c) [*Heermance et al.*, 2008]. In the core of the Kelatuo anticline above the fault, the Miocene strata are very deformed, creating numerous small-scale, tight folds (Figure 8d). Based on our field observations and the observations from seismic lines [*Heermance et al.*, 2008], the terrace appears to be deformed from movement on the underlying Atushi Fault (Figure 8d). The backtilting of the strath surface does not appear to coincide with any of the small-scale folds in the core of the Kelatuo anticline, which we assume formed prior to the translation of the Atushi/Kelatuo anticline above the Atushi Fault: an assumption supported by older (>5 Ma) burial cosmogenic ages from growth strata at the western end of the Kelatuo anticline [*Thompson*, 2013]. Therefore, we choose to use a listric thrust-fault model [*Amos et al.*, 2007] to calculate the shortening from the observed backtilting of the terrace and the geometry of the Atushi Fault from seismic data [*Heermance et al.*, 2008]. This model [*Amos et al.*, 2007] yields an estimated total shortening of ~86 m (Table 3). Applying simple line-length unfolding as a minimum value, the total shortening is ~2 m.

We collected two OSL samples from 8 to 31-cm-thick sand lenses preserved in gravels covering the bedrock strath. One sample, collected 16 m below the surface, yielded an age of 101.2 ± 10.6 ka, and the other sample, collected 31 m below the surface, was dated to 56.9 ± 8 ka (Tables 1 and 2). We interpret the older age to be incompletely bleached and discard it from further analyses for two reasons: (1) the ages are not in stratigraphic order and (2) regionally, previous work [*Li et al.*, 2012, 2013, 2015b; *Thompson*, 2013] indicates that the formation of the fill terrace above strath surfaces is typically climatically controlled [e.g., *Pan et al.*, 2003; *Huang et al.*, 2014], and terraces most commonly form and are abandoned during glacial-interglacial transitions. Several other terraces in the region date to ~55 ka [*Li et al.*, 2013]. Thus, we choose to use the younger age (56.9 ± 8 ka) and acknowledge this assumption results in a higher shortening rate estimate for the Atushi Fault.

Because the Atushi Fault is interpreted to flatten at depth (Figure 2c) [*Heermance et al.*, 2008], the total shortening rate following the listric fault model is $1.5^{+0.5}/_{-0.3}$ mm/yr (Table 4 and Figure 8c). Using simple line-length unfolding, the shortening rate is <0.1 mm/yr. Regardless of the exact underlying structure, the terrace records low to modest deformation on the Atushi Fault during the late Quaternary.

6. Late Quaternary Shortening Rates on the NE Pamir Margin

6.1. Fold Scarps of the Kenenbierte Thrust

The Kenenbierte Thrust (KT) and associated smaller faults deform an older alluvial fan to west of the town of Bieertuokuoyi (Figure 9). The fan is one of several older fans that once drained the northeast Pamir and are now abandoned and uplifted several hundred meters above the modern river channels. The surveyed fan lies ~140 m above the present-day river, displays a moderate desert pavement, and comprises cobble-boulder gravels with uncommon silt and sand lenses.

Quaternary alluvium, eroded from the uplifted fan surface, covers most of the underlying bedrock and prohibits a detailed interpretation of the structural geometry of the KT fault zone. Where exposed, we mapped the bedrock, which revealed several imbricate thrusts placing Eo-Oligocene sediments over the time-transgressive Xiyu Formation (Figures 9a and 9d). Near the northernmost fault scarp, a 45° south dipping blind fault cuts the Xiyu Formation. To the south of the fault, the Xiyu Formation rests unconformably over the Eo-Oligocene sediments, which are themselves locally thrust over the Xiyu Formation with >50 m of exposed offset. Approximately ~2.5 km farther south, a backthrust cuts these strata, before the section enters folded Eo-Oligocene sediments. Sparse structural measurements, poor exposure, and lack of correlatable beds prohibited a detailed interpretation of the subsurface structure. Thus, we were unable to confidently determine the underlying structure causing the deformation and instead used a simple line-length unfolding of the fan surface to constrain the minimum amount of deformation since fan abandonment.

Google Earth satellite image interpretation indicates multiple scarps displace the fan surface, some north-facing and others south-facing (Figure 9c), supporting the interpretation of multiple faults and folds that cause the deformation. Differential GPS surveys of the fan surface reveal a subtle warping (Figure 9d), with numerous scarps visible on the dGPS surveys (Figures 9d and 9e). These scarps and the warping
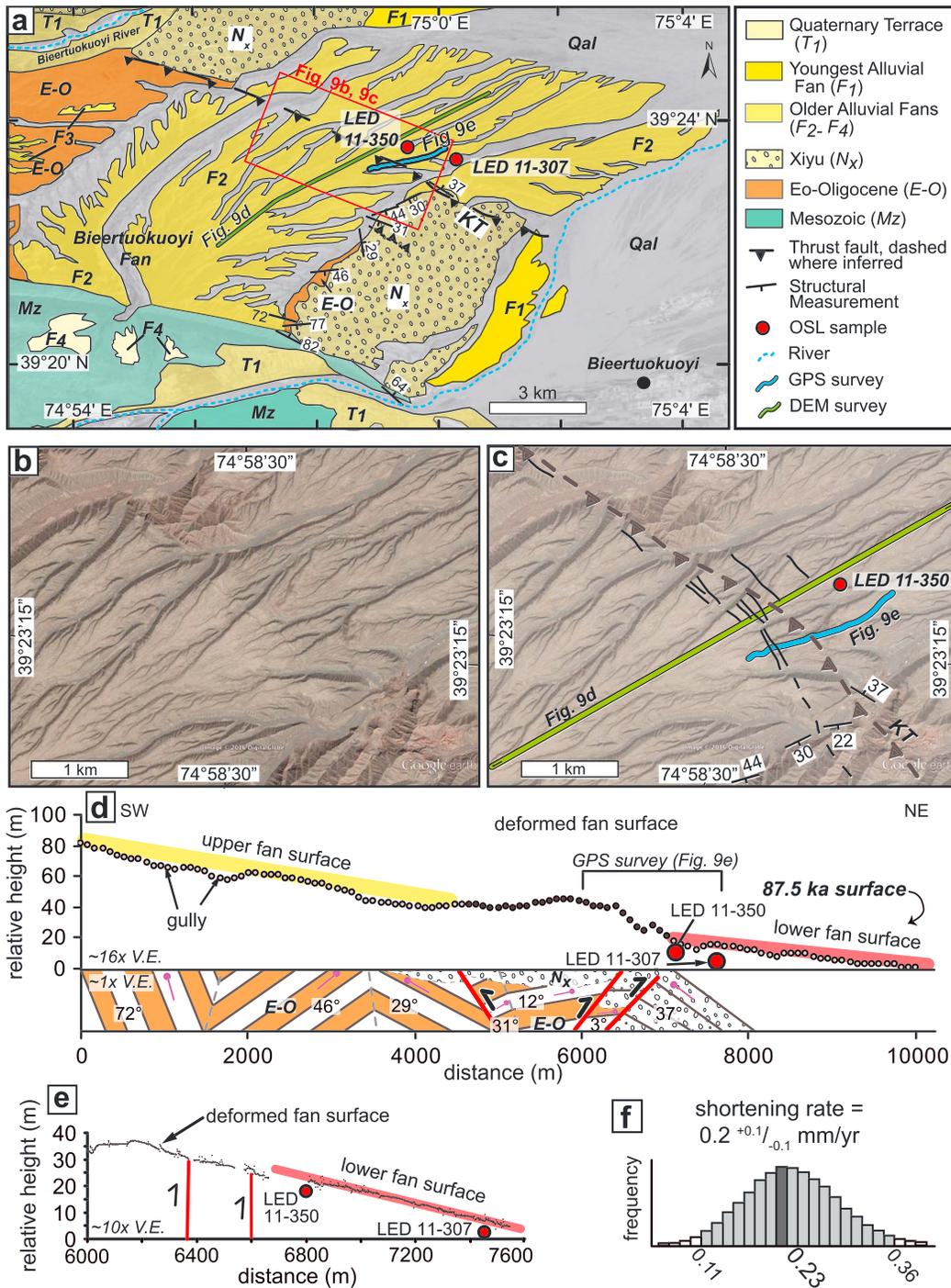
Figure 9. (a) Google Earth image with geomorphic map of the Bieertuokuoyi Fan. (b) Google Earth image and (c) geomorphic map of the Bieertuokuoyi Fan and associated fault scarps of the Kenenbierte Thrust. (d) SRTM90-DEM topographic profile of the fan surface, with exposed, mapped underlying faults and bedding. OSL sample locations marked by red circles. Location in Figures 9a and 9c. (e) dGPS topographic survey of the deformed section of the fan. Location in Figures 9a and 9c. (f) Shortening rate of the Kenenbierte Thrust (KT) calculated from line-length unfolding.

approximately coincide (±100 m) with mapped faults in the bedrock. Unfortunately, the extent of the deformed terrace surface was not obvious in the field, and our GPS surveys did not extend beyond the deformed section on the fan. Instead, we rely on a topographic profile extracted from the 90 m SRTM DEM coinciding with the dGPS survey. The warping of the fan is visible even at the lower spatial resolution of the DEM (Figure 9d) and broadly agrees with the GPS surveys of the same segment of the fan (Figure 9e). The total amount of shortening of the fan is ≥19.8 m (Table 3). Given the uncertainties associated with line-length unfolding, we assigned a 5 m error to the total shortening.

To date the fan's surface, two OSL samples (Table 1) were collected from fine sand-silt lenses 5–8 cm thick from depths of 4.5–50 m within the fan fill from the footwall of the fault zone. The samples yielded ages that generally agree with each other (Table 2), with a weighted mean depositional age of 87.5 ± 8.3 ka. Because these samples were collected from the footwall, which may have experienced continued deposition after initial uplift of the fan surface, we consider this age to be a minimum age. Using line-length unfolding, the estimated total shortening rate across the KT fault zone is estimated to 0.2 $^{+0.1}/_{-0.1}$ mm/yr (Table 4 and Figure 9f).

6.2. Fold Scarps of the Bieertuokuoyi Segment of the Pamir Frontal Thrust (PFT)

In the hanging wall of the PFT, three sets of preserved terraces record slip on the PFT during the Quaternary. The exposed bedrock north of the hinge beneath the highest terrace (Figure 10) dips ~62°. Because bedrock was not exposed south of the hinge, analogous dip data (mean = 50°) were projected along strike from a transect 4 km east. Because bedding can be easily traced along strike both in the field and in air photos, such a projection seems permissible.

In the field, we classified three deformed terraces (Figure 10) as fold scarps formed above a fault bend [e.g., *Chen et al.*, 2007b; *Hubert-Ferrari et al.*, 2007] based on the following key criteria. (1) We observed a change in the dip of the underlying sedimentary bedrock that approximately coincided with the change in slope on the terrace surface (Figure 10). Our observations and bedding measurements indicate that the structure can be well approximated by kink-style geometry, with panels of relatively consistent dips separated by narrow axial surfaces. (2) The change in slope of the terrace trends perpendicular to the adjacent modern river channels. This observation suggests that the changes in slopes on the three terraces are not terrace risers, because no field evidence is apparent for a river-channel avulsion that could explain the difference in channel orientation. (3) The change in slope observed at the base on all three deformed terraces spatially align with each other, which is unlikely if they do not share a common origin. (4) A seismic line through the PFT [*Xinlu et al.*, 2004; *Chen et al.*, 2010] indicates that the PFT and associated smaller faults have a complicated subsurface geometry, including several fault bends at depth (Figure 2b).

Six samples were collected to date the three terrace surfaces: four from T4 and two from T2a. The highest terrace, T4, has an age of 97.9 ± 5.5 ka from an average of four samples (Table 2). The lowest terrace, T2a, has an age of ~100 ka (Table 2). The OSL data from T2a indicate significant heterogeneous bleaching of silts in the lowermost terrace, with a wide scatter in natural luminescence and growth curves near saturation (Figure S1a). Based on the regional context of dated terraces, it seems highly unlikely that the abandonment age of a terrace only ~5 m above the modern river level would be ~100 ka. We interpret that these terraces should have similar ages to the terraces preserved nearby. Thus, we assign speculative ages of ~55 ka to T3, representing the MIS 4-3 transition (~57 ka), and ~14 ka to T2, representing the MIS 2-1 transition [*Lisiecki and Raymo*, 2005], consistent with regional terraces recognized within our field area [*Li et al.*, 2012, 2013; *Thompson*, 2013] and other areas on the margins of the western Tarim Basin [*Hubert-Ferrari*, 2005; *Huang et al.*, 2014]. We note that not all terrace ages in the region, however, correspond to climatic transitions [*Li et al.*, 2015b; *Bufe et al.*, 2017b], but T3 must be younger than T4, and T2a should be younger than T3, based on field observations and their relative positions above the modern riverbed. Given these uncertainties in the terrace ages, we assign a ± 10 ka error to the ages for T2a and T3.

Although all three terraces span the axial surface, only the highest one (T4) has a reliable age. This terrace has a scarp slope angle of 6° and a scarp height and length of 70 m and 720 m, respectively (Table 3 and Figure 10). The second highest terrace, T3, also has a scarp slope of 6°, and scarp height and length of T3 are 63 m and 480 m, respectively. T2a has a scarp slope of <~1°, a scarp height of 9 m, and a scarp length of ~330 m. The total slip recorded by T4, T3, and T2a is 540 m, 370 m, and 48 m, respectively (Table 3). Because slip along the PFT is likely transferred along a flat fault at the base of the Paleogene (E) at depth (Figure 2b) [*Chen et al.*, 2010; *Li et al.*, 2012],
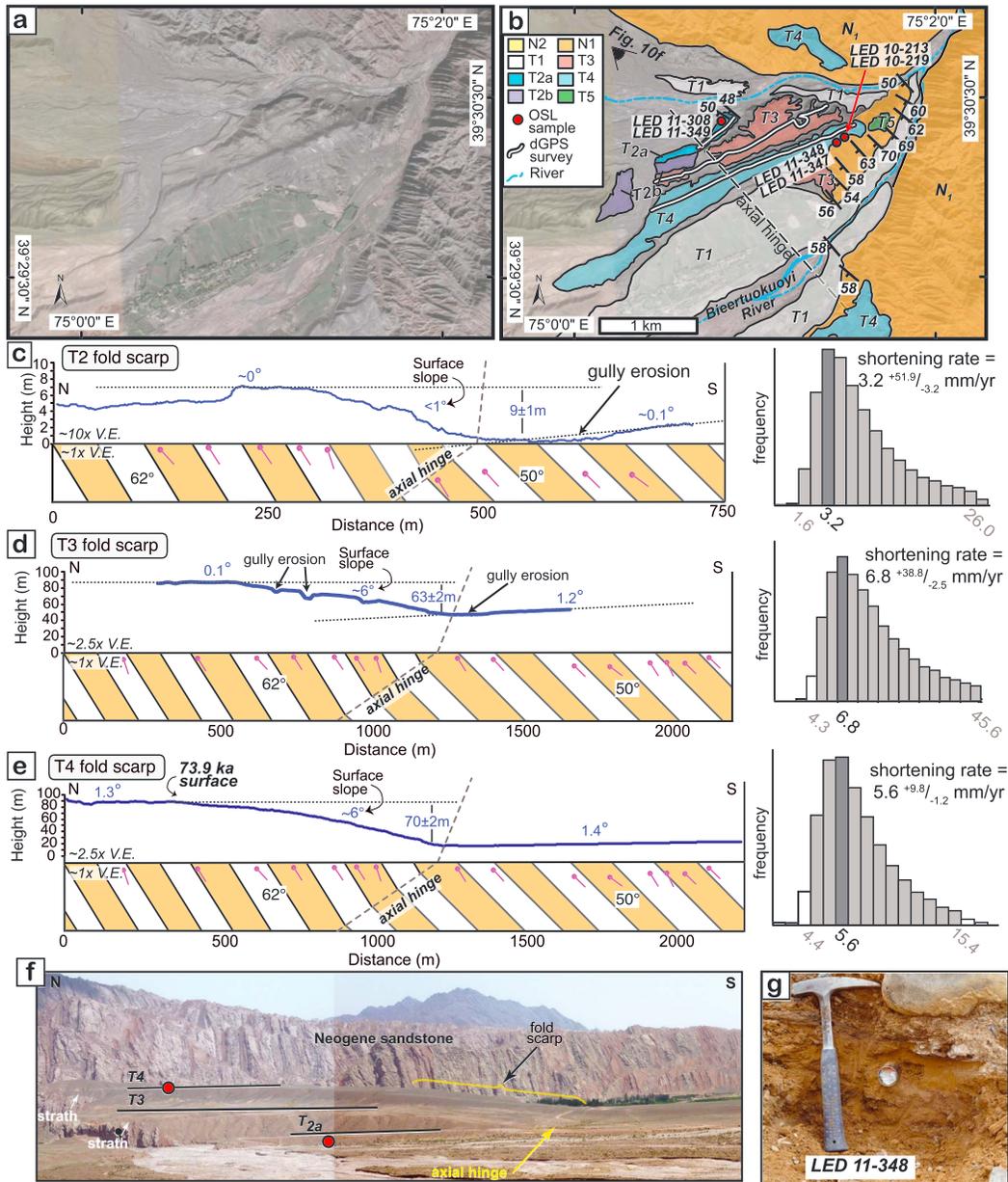
Figure 10. (a) Google Earth image and (b) geomorphic map of the Bieertuokuoyi fold scarps. dGPS topographic surveys of (c) T2a, (d) T3, and (e) T4 terraces and underlying Neogene structure, and their respective shortening rates. (f) Photo of the three fold scarps, looking east. Location in Figure 10b. (g) Photo of OSL sample LED 11-348 from T4.

the total slip recorded by the T4 scarp can be interpreted as an estimated shortening rate: $5.6^{+9.8}/_{-1.2}$ mm/yr for T4 (Table 4 and Figure 10). The estimated preliminary shortening rates for T3 and T2a are $6.8^{+38.8}/_{-2.5}$ and $3.2^{+51.9}/_{-3.2}$ mm/yr, respectively, pending better absolute age control (Table 3 and Figure 10).

6.3. Fold Scarps of the Aismaola Segment of the PFT

Located ~50 km farther east of Bieertuokuoyi, the Aismaola section of the PFT (Figure 1) has several flights of fluvial terraces (Figures 11a and 11b) that are beveled into Plio-Pleistocene growth strata, which dip ~8°SW (Figure 11c). We collected structural measurements from the underlying bedrock and a Chinese geologic
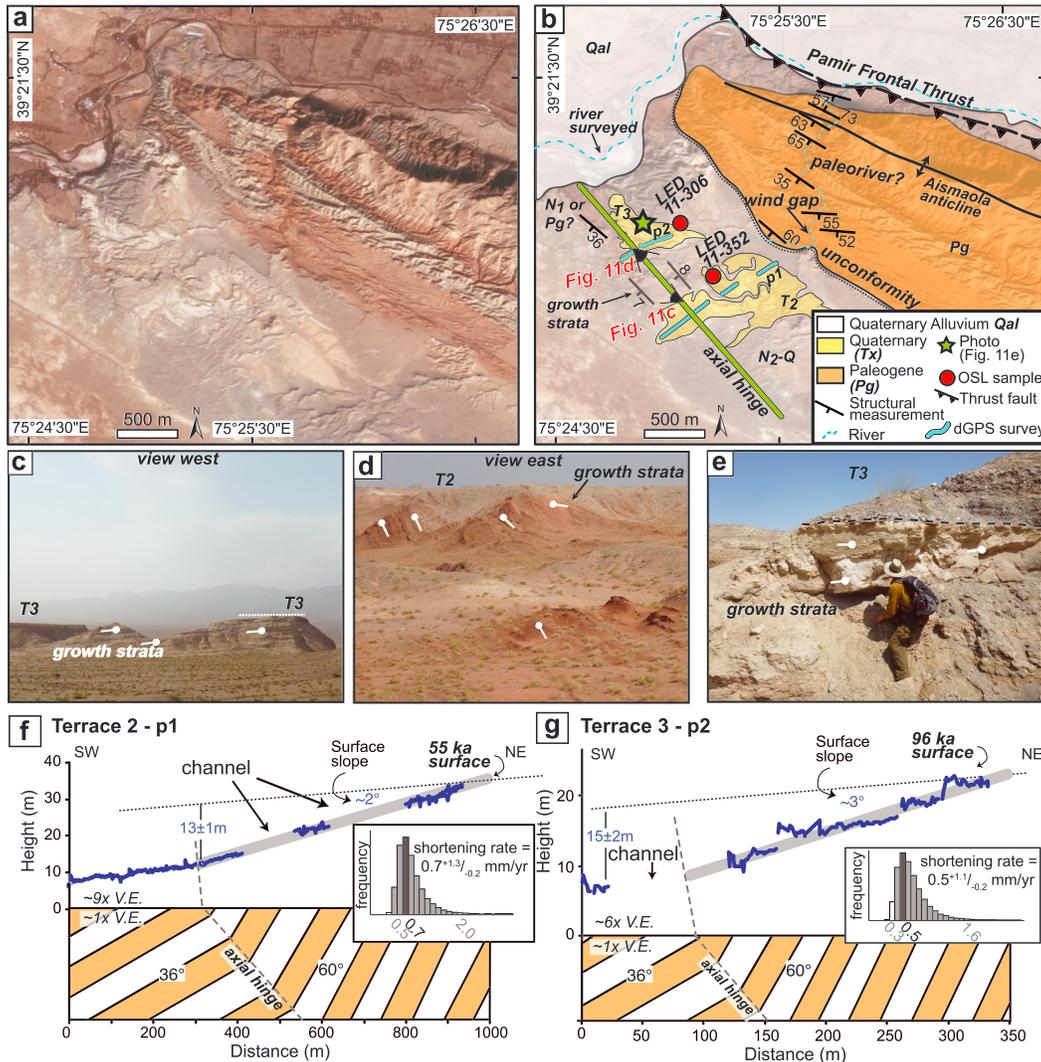
Figure 11. (a) Google Earth image and (b) geomorphic map of the Aismaola anticline. (c) Field photo of the T3 terrace. Plio-Pleistocene growth strata, dipping ~8° to the south, are under the terraces. Location in Figure 11b. (d) Field photo of the terraces, illustrating the discontinuous preserved surface. Location in Figure 11b. (e) Field photo of the T3 terrace and growth strata. Person for scale. Location is the green star in Figure 11b. (f) dGPS survey of T2, and minimum shortening rate. (g) dGPS survey of T3, and minimum shortening rate.

map [*Xinjiang Bureau of Geology and Mineral Resources*, 1993]. Although poor exposure of the underlying bedrock hinders a reliable interpretation of its structure, a localized change in dip of the underlying Paleogene bedrock from 36° to 60° is observed. Differential GPS surveys of each deformed terrace indicate that the surfaces are backtilted approximately 2–3° to the southwest. The change in dip of the terrace surface is located within a zone between the change in dips of the underlying bedrock, and therefore, we classify this fold as a fault-bend fold and calculate shortening following a fold scarp model (Table 3) [*Thompson et al.*, 2002; *Chen et al.*, 2007b]. This interpretation is supported by seismic reflection data near the Aismaola anticline (Figures 1 and 2a) [*Chen et al.*, 2010; *Cheng et al.*, 2016]. Furthermore, the underlying fault on the anticline's northern limb (PFT, Figure 11) offsets undated late Quaternary alluvial deposits, creating a scarp ~50–75 cm high with lateral offsets of ~1–1.5 m [*Fu et al.*, 2010].

The terrace surfaces presently lie 30–45 m above the modern river. The cover of the strath terrace is a thin (0.5 m to 5 m) layer of unconsolidated cobbles and gravels with common laminated silt and sand lenses
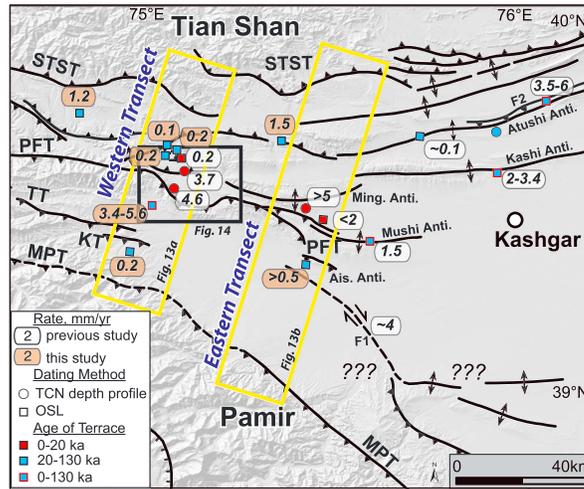
Figure 12. Simplified structural map of the western Tarim Basin, with approximate shortening rates of major faults and folds [*Shen et al.*, 2001; *Fu et al.*, 2010; *Li*, 2012; *Li et al.*, 2012, 2013, 2015b; *Thompson*, 2013; *Yang*, 2013; *Bufe et al.*, 2017a, 2017b]. New rates are shown in tan ovals, and rates from previous studies are shown as white ovals. Black box marks location of map in Figure 14. Blue rectangles mark eastern and western transects shown in Figure 13. MPT = Main Pamir Thrust, KT = Kenenbierte Thrust, TT = Takegai Thrust, PFT = Pamir Frontal Thrust, and STST = South Tian Shan Thrust.

(Figures 11c and 11e). The terrace surface has weakly developed desert pavement, although clasts have a dark desert varnish.

The lower terrace, T2, is backtilted ~2° to the SW and has a preserved discontinuous surface tread (Figure 11f). The upper surface tread of the fold scarp is not preserved. The higher terrace, T3, is backtilted ~3.2° to the SW and has a similar discontinuous surface, with small channels creating an uneven tread even where it is preserved (Figures 11d and 11g). For both terraces, we assume the upper terrace tread must have had a similar initial depositional slope as the lower terrace tread [*Chen et al.*, 2007b] and acknowledge the deformation recorded here is a minimum given that we do not know how much of the fold scarp has been eroded and we cannot constrain its total length. However, minimum shortening magnitudes based on the preserved terrace treads are >44 m and >55 m for T2 and T3 (Table 3), respectively.

We assume a river draining to the north/northeast across or around the Aismaola anticline deposited the terraces, and we choose to use the modern river to the northwest of the terraces (Figure 11b) as a marker to compare the terrace deformation. This interpretation is supported by three main observations. First, limited clast imbrications support a paleoflow from the south/southwest to north/northeast. Second, the terrace gravels include granite and limestone clasts, which cannot be derived from the growing anticline that is composed of sandstones and siltstones. Finally, a wind gap exists in the anticline to the north of the terraces and suggests that a river once flowed across the fold in the vicinity of the terraces. Given these observations, the terraces are unlikely to be formed by a river draining south from the Aismaola anticline. If, however, instead of the assumed northeast drainage, a southeast flowing axial river formed the terraces as the river was diverted around the growing anticline, then the original terrace gradients in the direction of shortening (SW/NE) would be minimal, and the present-day terrace slopes would result primarily from deformation on the underlying structure.

We collected two OSL samples, one from each terrace surface, to constrain the depositional ages of the terraces (Tables 1 and 2). The sample from T2, collected from a laminated silt lens 1 m below the lower terrace surface, yielded an age of 55 ± 8 ka. The sample from the higher terrace, T3, collected from a silt lens with a depth of 1.5 m, yielded an age of 96 ± 11.9 ka. These ages yield minimum slip rates of 0.7 $^{+1.3}/_{-0.2}$ mm/yr and 0.5 $^{+1.1}/_{-0.2}$ mm/yr for T2 and T3 (Table 4 and Figures 11f and 11g), respectively. Because the PFT is interpreted to nearly flatten at depth (~10–20° dip) on regional seismic lines [*Chen et al.*, 2010] (Figure 2a), the slip rates can be approximated as minimum shortening rates. Given the many uncertainties associated with both the surveys and the underlying structure, absolute rates remain poorly defined, but our data and observations demonstrate that the anticline has been actively growing during the late Quaternary.

7. Discussion

7.1. Spatial Patterns of Shortening in the Pamir-Tian Shan Convergence Zone

Quaternary deformation rates on faults and folds in the western Tarim Basin (Table 4 and Figure 12) indicate that the locus of deformation is not concentrated on a single fault, but rather, strain is distributed across a zone at least 60 km wide along the interface of the Pamir and Tian Shan orogens (Figure 12, Figure 13). In
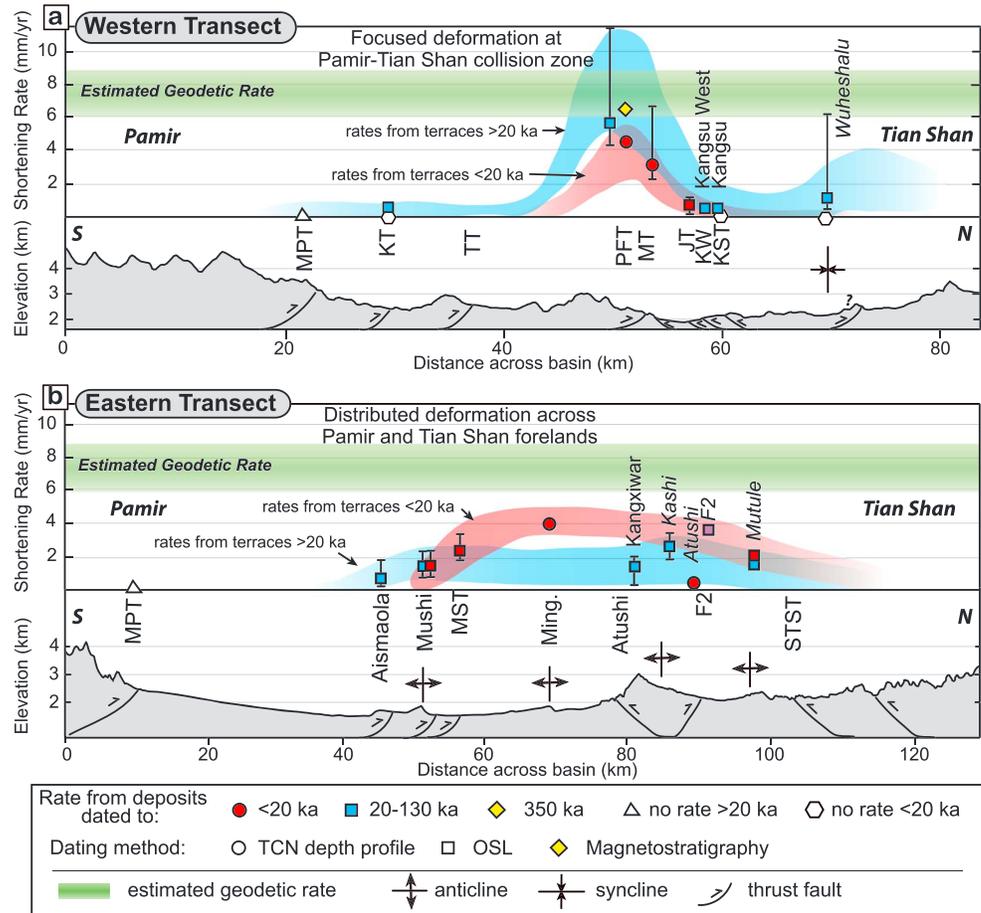
Figure 13. (a) Western transect and (b) eastern transect across the Pamir-Tian Shan forelands (see transect locations in Figure 12). Top panel shows estimated deformation rates on each dated structures. Circles are rates derived from TCN depth profile dating, squares are rates derived from OSL dating, and diamonds are rates derived from magnetostratigraphic dating. Red symbols are surfaces <20 ka, blue symbols are surfaces 20–130 ka, and yellow symbols are deposits 350 ka. White symbols represent no observable activity at <20 ka (polygon) or >20 ka (triangles). Green shaded bar represents the approximate geodetic rates across the region [*Mohadjer et al.*, 2010; *Li et al.*, 2012; *Ischuk et al.*, 2013]. Rates and errors are from Table 4. Bottom panels show an elevation profile across the foreland, with the approximate location of major faults and folds. Kashi, Atushi, and Mutule anticlines, fault F2, and Wuheshalu locations are projected onto transect and are approximate. Fault F2 (purple square) is displayed for reference, but rates are not included in the total shortening across the region. Note along the western transect, deformation is focused at the Pamir-Tian Shan collision zone, whereas along the eastern transect, where the orogens are just beginning to impinge, deformation is more distributed across faults and folds spanning the foreland. MPT = Main Pamir Thrust, KT = Kenenbierte Thrust, TT = Takegai Thrust, PFT = Pamir Frontal Thrust, STST = South Tian Shan Thrust, MST = Mingyaole South Thrust, MT = Mayikake Thrust, and JT = Jilegeyoute Thrust.

general, the most active faults during the late Quaternary are located near the leading edge of the Pamir orogen (Figure 13a), but active structures appear to be more distributed across the Tian Shan margin (Figure 13b). Although additional age data on undated deformed terraces are needed to illuminate more detail, several general patterns emerge:

1. On the Tian Shan margin, deformation appears to be more distributed across the foreland throughout the Quaternary, although structures closest to the mountain fronts are generally less active during the latest Quaternary (Figure 13b).

   Along the western part of the margin (Figure 12), older terraces (>20 ka) record modest deformation, but little discernible deformation is apparent on younger terraces (<20 ka). For example, the older T2 terraces

(~40 ka) at Wuheshalu are clearly deformed into fold scarps (Figure 4c). Younger terraces here reveal no discernable fold scarps, indicating recent limited activity of the structure (Figure 4e). At Kangsu, only older terraces (~120 ka) record even modest deformation on the Kangsu South Thrust (Figure 5) and the Kangsu West Fault Zone (Figures 6 and 7). The Kangsu South Thrust has likely accommodated a significant amount of shortening during the Neogene, yet the small scarps and lack of offset features on the younger terraces indicate limited fault movement during the late Quaternary. Alternatively, a long (thousands of years) earthquake recurrence interval, similar to those observed on some other faults in Central Asia [*Abdrakhmatov et al.*, 2016; *Grützner et al.*, 2017], and erosional processes may mask the true activity of the fault by removing or modifying the surface expression of faulting. The distributed fault scarps within the Kangsu West Fault Zone farther south on the same broad terrace (Figures 5b, 6, and 7) suggest that deformation has migrated southward during the latest Quaternary and is partitioned onto strike-slip and thrust faults.

Along the eastern part margin in the Kashi-Atushi fold-and-thrust belt (Figure 12), shortening rates are inferred primarily from rock-uplift rates and limited dGPS surveys across folds. Deformation is lower on hinterland structures but is generally more distributed across the foreland over late Quaternary time-scales. For example, terraces crossing the Keketamu anticline (Figure 1), a hinterland structure in the northern Kashi-Atushi foreland, record modest (<1 m) deformation [*Heermance et al.*, 2008]. Farther south into the foreland, line-length unfolding of terraces crossing the Atushi anticline at a water gap east of Kangxiwar record a total shortening of ~11 m and an estimated shortening rate of ~1 mm/yr [*Heermance et al.*, 2008]. However, recent work suggests the anticline may be shortening at a slower rate of ~0.1 mm/yr (Figure 12), based on a ^{10}Be cosmogenic depth profile age of ~82 ± 22 (2σ) ka [*Bufe et al.*, 2017b]. Although line-length unfolding may be less robust than other methods, good agreement exists between the excess-area method and line-length unfolding when calculating shortening rates across the detachment folds in the Kashi-Atushi fold-and-thrust belt when the entire structure is considered [*Scharer et al.*, 2004]. The Kashi and Mutule anticlines have estimated rock-uplift rates of 2–3.4 mm/yr (over the past 40–50 kyr) and 1.4–2.4 mm/yr (over the past 11–30 kyr), respectively, from dating of deformed terraces crossing the anticlines [*Bufe et al.*, 2017b]. If we assume that rock-uplift rates are approximately equal to the shortening rates of detachment folds [*Poblet and McClay*, 1996], suggested as an end-member model if the folds deform primarily by hinge migration [*Scharer et al.*, 2006], then the estimated shortening rates for the Kashi and Mutule folds are 2–3.4 mm/yr and 1.4–2.4 mm/yr, respectively. At Atushi anticline, however, the shortening rate from line-length unfolding of a deformed terrace (~0.1 mm/yr) is much less than the uplift rate (~0.7–1.3 mm/yr) [*Bufe et al.*, 2017b], suggesting that the folds do not deform by pure hinge migration. Thus, the geologic shortening rates at Kashi and Mutule anticlines that are based on rock-uplift rates are interpreted to be maximum late Quaternary shortening rates, because the folds likely deform by a combination of limb rotation and hinge migration [*Scharer et al.*, 2006], which results in a shortening rate that is less than the rock-uplift rate.

2. Along the NE Pamir, we did not observe any evidence for rapid (>1 mm/yr) slip on the Main Pamir Thrust (MPT) or the Kenenbierte Thrust (KT) during the late Quaternary (Figure 13a). No scarps or offset late Quaternary geomorphic features are associated with the MPT, the major range-bounding fault. However, rapid erosion and deposition of fans along the mountain front may have erased any scarps that formed in recent times. In the field, we did observe uplifted and tilted fans that are of possible late Quaternary age near the MPT, but were unable to sample or survey them due to field access. A cosmogenic burial age (~2.2 Ma) from older growth strata related to the fault suggests the fault was active during the earliest Quaternary [*Thompson*, 2013]. Along the Kenenbierte Thrust (KT), the next fault into the foreland (Figure 1), the shortening rate averages ~0.2 mm/yr since ~87 ka (Figure 9), and younger fans (<87 ka) crossing the thrust record negligible recent deformation. These modest rates on hinterland structures also suggest that, although they may still be active, the main deformation front has propagated northward to the Pamir Frontal Thrust (PFT) (Figure 13a).

3. Structures within the foreland at the leading edge of both orogens and within the Pamir-Tian Shan convergence zone record rapid Quaternary deformation (> ~1 mm/yr) since at least ~150 ka (Figures 13b and 14). Deformed terraces crossing the Mushi anticline (Loc. 2, Figure 1), ranging in age from 15 to 130 ka, indicate the fold is shortening at a uniform rate of ~1.5 mm/yr (Figures 12 and 15) [*Li et al.*, 2013]. To the north of the Mushi anticline, deformed fold scarps on the southern flank of the Mingyaole anticline (Loc. 4 and Loc. 7, Figure 1) indicate the fold is shortening at a rate of ~1.2 mm/yr, and similar-
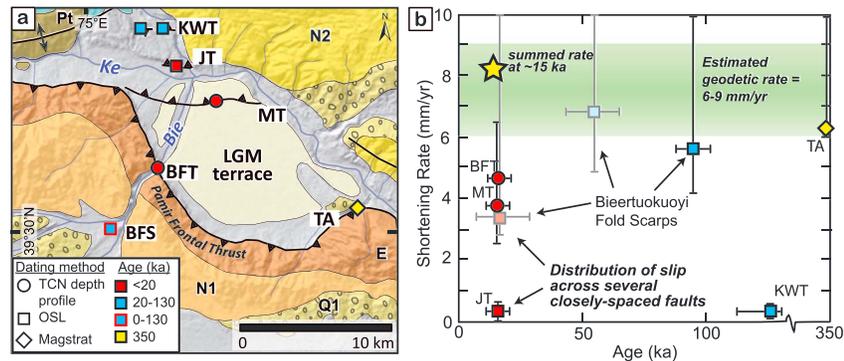
Figure 14. (a) Simplified geologic map of the Pamir Frontal Thrust near the Mayikake Basin. Symbols are the same as in Figure 13. (b) Change in shortening rates on the PFT since ~350 ka [*Li*, 2012; *Li et al.*, 2012; *Thompson*, 2013; this study]. Blue shaded squares represent estimated rates from Bieertuokuoyi fold scarps. Green shaded bar represents approximate geodetic rate across the region. Note nearly constant shortening rate since ~350 ka to the present, although deformation appears to be distributed across several closely spaced faults since ~15 ka. MT = Mayikake Thrust, JT = Jilegeyoute Thrust, BFT = Bieertuokuoyi segment of the Pamir Frontal Thrust, BFS = Bieertuokuoyi Fold Scarps, TA = Tuomuluoan Anticline, Bie = Bieertuokuoyi River, and Ke = Kezilesu River.

sized fold scarps on the northern flank may indicate the shortening rate is as high as 5 mm/yr [*Thompson*, 2013; *Li et al.*, 2015b]. Numerous older terraces crossing the structure indicate the fold has been active throughout the late Quaternary [*Scharer et al.*, 2006; *Li et al.*, 2015b]. Furthermore, at the Aismaola anticline, at least two flights of terraces are deformed, recording shortening rates of >0.5 to >0.7 mm/yr (Figure 11). These lower shortening rates at Aismaola may be complemented by deformation on the unnamed strike-slip fault F1 ~ 10 km to the south that accommodates ~4.0 mm/yr of northward movement (Loc. 8, Figure 1) [*Fu et al.*, 2010]. Farther west, near the Mayikake basin, the Bieertuokuoyi

Frontal Thrust (BFT) and Mayikake Thrust (MT) have rates of ~4.6 and ~3.7 mm/yr (Loc. 1, Figure 1) [*Thompson*, 2013], whereas the Jilegeyoute Thrust (JT) on the Tian Shan side of the collision zone has a lower rate of ~0.2 mm/yr since ~14 ka (Loc. 3, Figure 1; Figure 11) [*Li*, 2012].

7.2. Contrasting Distribution of Shortening in the Pamir and Tian Shan

From these data, the Pamir orogen is most active at its leading edge, with modest deformation in the hinterland, whereas deformation across the margin of the Tian Shan appears to be more distributed, with similar rates on structures at the leading edge of the orogen as on more hinterland structures (Table 4 and Figures 12–14). These data also allow us to speculate that at the western end of the Tarim Basin where the Pamir and Tian Shan are already juxtaposed, most of the deformation is accommodated along the Pamir Frontal Thrust, such
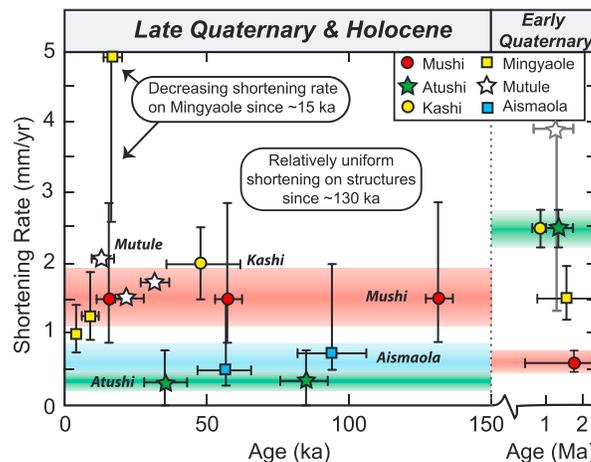

Figure 15. Summary of shortening rates across structures in the eastern transect area from previous studies, illustrating relatively uniform shortening across structures since ~150 ka [*Li et al.*, 2013, 2015b; *Bufe et al.*, 2017b]. To the right of the black vertical dashed line, the average shortening rates of the folds since their initiation in the Early Quaternary are shown [*Scharer et al.*, 2004; *Chen et al.*, 2005; *Heermance et al.*, 2008; *Li et al.*, 2013; *Thompson*, 2013; *Bufe et al.*, 2017a, 2017b], with the estimated errors on the rate from Mutule shown in grey. The shortening rates of several folds changed through time as the locus of deformation shifted during the Quaternary.

that limited recent deformation occurs on structures on the Tian Shan side of the convergence zone or on more hinterland structures in the Pamir (Figure 13a), although long recurrence intervals on faults and erosion processes may complicate the interpretation of the true activity of the hinterland structures [*Grützner et al.*, 2017]. Farther east, where the two orogens are more widely separated and the Tarim Basin itself is just beginning to deform, deformation is spread across multiple foreland structures (Figures 13b and 15). This interpretation is most evident in the Kashi-Atushi fold-and-thrust-belt, where active deformation is clearly recorded by fault scarps and folded terraces across the foreland [*Shen et al.*, 2001; *Scharer et al.*, 2006; *Heermance et al.*, 2008; *Fu et al.*, 2010; *Bufe et al.*, 2017b]. Similarly, deformation is manifested in the generally higher topography across the foreland compared to the Pamir foreland at a similar longitude (Figure 13b). On the Pamir side, deformation is spread across three main structures: the Mingyaole, Mushi, and Aismaola anticlines, and slip is distributed between these three structures. Furthermore, the few mapped strike-slip faults may play an important role in accommodating the northward shortening, especially along the margin of the Pamir. The PFT, F1, and the Kangsu West Fault Zone record modest to fast (~0.5–5 mm/yr) dextral slip rates.

7.3. Temporal Patterns of Shortening in the Pamir-Tian Shan Collision Zone

Importantly, although numerous structures accommodate the shortening throughout the Quaternary and the loci of deformation shift through time, the total shortening rate across the western Tarim Basin appears to have remained relatively uniform since ~0.35 Ma [*Li et al.*, 2012] and likely throughout the entire Quaternary (Table 4 and Figures 13–15). In the western area, the Pamir Frontal Thrust had an average slip rate of 10–12 mm/yr since its initiation 5–6 Ma [*Thompson et al.*, 2015]. The late Quaternary slip rate of ~5.6 mm/yr from the hanging wall of the Pamir Frontal Thrust (PFT) is comparable to the slip rate of >6.4 mm/yr calculated on the PFT farther to the east at the Tumouluoan Thrust (Loc. 1, Figure 1) [*Li et al.*, 2012] over Quaternary (50–350 ka) timescales. During the latest Quaternary, the Bieertuokuoyi Frontal Thrust (BFT) has a slip rate of only 4.6 mm/yr [*Li et al.*, 2012; *Thompson*, 2013], which is similar to the estimated rate (~3.2 mm/yr) on the Bieertuokuoyi fold scarps of the same probable age. Farther to the north, the Mayikake Thrust (MT) also cuts the Last Glacial Maximum surface and has a slip rate of 3.7 mm/yr [*Li et al.*, 2012; *Thompson*, 2013]. Thus, the sum of latest Pleistocene and Holocene (~20 ka to present) shortening across this zone (8.5 mm/yr) is similar to the slip rates (7.6 mm/yr, >6.4 mm/yr, and 10–12 mm/yr) over Quaternary/Pliocene timescales (75 ka, 350 ka, and 5–6 Ma, respectively), thereby suggesting steady shortening on the PFT zone since its initiation, even though shortening was accommodated on different structures within the narrow PFT zone through time (Table 4 and Figure 14). This rate is also broadly comparable to the modern geodetic shortening rate of ~6–9 mm/yr across the PFT calculated from GPS stations in the Pamir and Tian Shan [*Mohadjer et al.*, 2010; *Zubovich et al.*, 2010; *Ischuk et al.*, 2013; *Zubovich et al.*, 2016].

In the eastern area where the Tian Shan and Pamir remain separated across the lateral tapering Tarim Basin, shortening was spatially distributed across folds in the foreland during the Quaternary. However, the loci of deformation changed through time, with individual structures recording changing rates from the early to late Quaternary [*Bufe et al.*, 2017a]. For example, the Atushi anticline has an average shortening rate between 2.25 and 2.75 mm/yr since initiation 1–1.4 Ma [*Heermance et al.*, 2008], whereas the late Quaternary rate since ~80 ka is much lower: ~0.1 mm/yr. The Mushi anticline has an average shortening rate of ~0.6 mm/yr since its initiation ~1.3 Ma [*Thompson*, 2013], but the average shortening rate increased since ~130 ka and appears to have remained steady at ~1.5 mm/yr [*Li et al.*, 2013]. The Mingyaole anticline also has an increased shortening rate in the late Quaternary, with a shortening rate since ~15 ka of >5 mm/yr [*Li et al.*, 2015b; *Thompson*, 2013], whereas the shortening rate since initiation at ~1.6 Ma is between 1.1 and 1.9 mm/yr [*Chen et al.*, 2005]. In contrast, the Mutule anticline records a decreasing uplift (and likely shortening) rate through time [*Bufe et al.*, 2017a], whereas the Kashi anticline appears to have a uniform Quaternary shortening rate (within error) between 2 and 3.5 mm/yr [*Scharer et al.*, 2004; *Heermance et al.*, 2008; *Bufe et al.*, 2017a, 2017b].

7.4. Transfer of Deformation Into the Foreland

The transfer of shortening to faults and folds closer to the foreland appears to be facilitated by the evaporite detachment horizons within the Paleogene and Miocene foreland strata [Figure 2; *Scharer et al.*, 2006; *Heermance et al.*, 2008; *Wang et al.*, 2016]. A gypsiferous horizon in the Paleogene Aertashi Formation serves as a detachment for the PFT, and interpretations from regional seismic lines and analogue modeling suggest that this weak zone transfers most of the shortening from the range-bounding faults to the frontal faults at depth (~6 km depth) [*Xinlu et al.*, 2004; *Chen et al.*, 2010; *Wang et al.*, 2016]. Recent analogue modeling shows

that patterns of major faults can be influenced by preexisting uplifted basement structures [*Wang et al.*, 2016], which may serve as a rigid backstop for the Pamir margin. On the southern Tian Shan margin, however, the evaporite detachment is interpreted to be more distributed throughout the Miocene Wuqia Group C [*Heermance et al.*, 2008], creating detachment folds in the Kashi and Atushi fold-and-thrust belt [Figure 2; *Scharer et al.*, 2006; *Heermance et al.*, 2008; *Bufe et al.*, 2017b]. Thus, a discrete, localized evaporite decollement within the Paleogene may focus the deformation front on the NE margin of the Pamir to a single fault zone, whereas along the southern Tian Shan margin, the lack of an efficient, regionally extensive evaporite horizon across the orogen front may lead to more distributed deformation. This interpretation is supported by Quaternary shortening rates on the structures, with the PFT accommodating much of the northward movement of the Pamir since 0.35 Ma (Figures 13a and 14). However, over longer timescales, both out-of-sequence thrusting and coeval thrusting occur along the margins of both the Pamir [*Thompson et al.*, 2015] and Tian Shan [*Scharer et al.*, 2004; *Heermance et al.*, 2008], suggesting a different pattern of strain partitioning in more recent times (Table 4).

The focus of deformation along the Pamir-Tian Shan interface may also be a response to localized erosion from the Kezilesu River. Although the role of active erosion controlling deformation is still debated [*Avouac*, 1996; *Whipple*, 2009], numerical models suggest focused and localized erosion may enhance and accelerate deformation [*Koons and Kirby*, 2007], such as along the leading edge of an orogen [*Zeitler et al.*, 2001; *Koons et al.*, 2002]. Enhanced fluvial erosion during the late Quaternary climatic cycles [*Molnar and England*, 1990] may have focused deformation along the river corridor, causing the deformation front to propagate toward and then persist along the Pamir-Tian Shan interface. Localized erosion would affect the western transect, where the Kezilesu River is trapped between the Pamir and Tian Shan (Figure 13a), but would not affect the eastern transect, where the Tarim Basin widens and more distributed, transverse rivers cross the structures and limit focused erosion (Figure 13b). Definitively determining that fluvial erosion focuses the deformation is beyond the scope of this study, but could be an avenue for future research.

8. Conclusions

Rapid and persistent convergence between the Pamir and Tian Shan in western China facilitate an illuminating quantification of the pattern and rates of Quaternary deformation that reveal two contrasting responses to the ongoing convergence. Using geologic and geomorphic mapping, dGPS surveys of deformed terraces, and OSL dating, we create a synthesis of the active structures that delineate the timing, rate, and migration of Quaternary deformation during ongoing convergence. In this study, we present new shortening rates on eight faults and folds, which we combined with previous work in the region to determine spatial and temporal patterns of Quaternary deformation. In the westernmost Tarim Basin, the fastest rates (6–9 mm/yr) are currently focused on actively deforming structures at the interface of the Pamir-Tian Shan orogens. Here, shortening rates have remained fairly steady since the Pliocene (~4–6 Ma). The Quaternary deformation rates farther east indicate that the locus of deformation has not been concentrated on a single structure or orogenic zone but rather was concurrently distributed across a swath of structures in the Kashi-Atushi fold-and-thrust belt, with individual structures exhibiting variable shortening rates since ~2 Ma. Although numerous structures have accommodated the shortening and the locus of deformation has shifted during the Quaternary, the total shortening across the western Tarim Basin has remained uniform and is approximately equal to the current geodetic rate of 6–9 mm/yr.

References

Abdrakhmatov, K. E., et al. (2016), Multisegment rupture in the 11 July 1889 Chilik earthquake (M_w 8.0–8.3), Kazakh Tien Shan, interpreted from remote sensing, field survey, and paleoseismic trenching, *J. Geophys. Res. Solid Earth*, *121*, 4615–4640, doi:10.1002/2015JB012763.
Amidon, W. H., and S. A. Hynek (2010), Exhumational history of the north central Pamir, *Tectonics*, *29*, TC5017, doi:10.1029/2009TC002589.
Amos, C. B., D. W. Burbank, D. C. Nobes, and S. A. L. Read (2007), Geomorphic constraints on listric thrust faulting: Implications for active deformation in the Mackenzie Basin, South Island, New Zealand, *J. Geophys. Res.*, *112*, B03S11, doi:10.1029/2006JB004291.
Armstrong, F. C., and S. S. Oriel (1965), Tectonic development of Idaho-Wyoming thrust belt, *AAPG Bull.*, *49*(11), 1847–1866.
Arrowsmith, J. R., and M. R. Strecker (1999), Seismotectonic range-front segmentation and mountain-belt growth in the Pamir-Alai region, Kyrgyzstan (India-Eurasia collision zone), *Geol. Soc. Am. Bull.*, *111*(11), 1665, doi:10.1130/0016-7606(1999)111<1665:SRFSAM>2.3.CO;2.
Avouac, J. P. (1996), Erosion as a driving mechanism of intracontinental mountain growth, *J. Geophys. Res.*, *101*, 17,747–17,760.
Bufe, A., D. Bekaert, E. Hussain, B. Bookhagen, D. W. Burbank, J. A. Thompson Jobe, J. Chen, T. Li, L. Liu, and W. Gan (2017a), Temporal changes in rock-uplift rates of folds in the foreland of the Tian Shan and the Pamir from geodetic and geologic data, *Geophys. Res. Lett.*, *44*, doi:10.1002/2017GL073627.

Bufe, A., D. W. Burbank, L. Liu, B. Bookhagen, J. T. Qin, J. Chen, T. Li, J. A. Thompson Jobe, and H. L. Yang (2017b), Variations of lateral bedrock erosion rates control planation of uplifting folds in the foreland of the Tian Shan, NW China, *J. Geophys. Res. Earth Surf.*, *122*, doi:10.1002/2016JF004099.

Burbank, D. W., and R. G. H. Reynolds (1984), Sequential late Cenozoic structural disruption of the northern Himalayan foredeep, *Nature*, *311*, 114–118.

Burtman, V. S., and P. Molnar (1993), Geological and geophysical evidence for deep subduction of continental crust beneath the Pamir, *Geol. Soc. Am. Spec. Pap.*, *281*, 1–76.

Cao, K., M. Bernet, G.-C. Wang, P. van der Beek, A. Wang, K.-X. Zhang, and E. Enkelmann (2013a), Focused Pliocene–Quaternary exhumation of the Eastern Pamir domes, western China, *Earth Planet. Sci. Lett.*, *363*, 16–26, doi:10.1016/j.epsl.2012.12.023.

Cao, K., G.-C. Wang, P. van der Beek, M. Bernet, and K.-X. Zhang (2013b), Cenozoic thermo-tectonic evolution of the northeastern Pamir revealed by zircon and apatite fission-track thermochronology, *Tectonophysics*, *589*, 17–32, doi:10.1016/j.tecto.2012.12.038.

Carroll, A. R., S. A. Graham, M. S. Hendrix, D. Ying, and D. Zhou (1995), Late Paleozoic tectonic amalgamation of northwestern China: Sedimentary record of the northern Tarim, northwestern Turpan, and southern Junggar Basins, *Geol. Soc. Am. Bull.*, *107*(5), 571–594, doi:10.1130/0016-7606(1995)107<0571:LPTAON>2.3.CO;2.

Cavalié, O., and S. Jónsson (2014), Block-like plate movements in eastern Anatolia observed by InSAR: Tectonics in Eastern Anatolia, *Geophys. Res. Lett.*, *41*, 26–31, doi:10.1002/2013GL058170.

Charreau, J., S. Gilder, Y. Chen, S. Dominguez, J.-P. Avouac, S. Sen, M. Jolivet, Y. Li, and W. Wang (2006), Magnetostratigraphy of the Yaha section, Tarim Basin (China): 11 Ma acceleration in erosion and uplift of the tian Shan mountains, *Geology*, *34*(3), 181–184.

Charreau, J., C. Gumiaux, J.-P. Avouac, R. Augier, Y. Chen, L. Barrier, S. Gilder, S. Dominguez, N. Charles, and Q. Wang (2009), The Neogene Xiyu Formation, a diachronous prograding gravel wedge at front of the Tianshan: Climatic and tectonic implications, *Earth Planet. Sci. Lett.*, *287*(3–4), 298–310, doi:10.1016/j.epsl.2009.07.035.

Chen, H. L., F. F. Zhang, X. G. Cheng, L. Liao, J. C. Luo, J. Shi, B. Q. Wang, C. F. Yang, and L. F. Chen (2010), The deformation features and basin-range coupling structure in the northeastern Pamir tectonic belt, *Chin. J. Geol.*, *45*(1), 102–112.

Chen, J., D. W. Burbank, K. M. Scharer, E. Sobel, J. Yin, C. Rubin, and R. Zhao (2002), Magnetochronology of the Upper Cenozoic strata in the southwestern Chinese Tian Shan: Rates of Pleistocene folding and thrusting, *Earth Planet. Sci. Lett.*, *195*(1), 113–130.

Chen, J., K. M. Scharer, D. W. Burbank, R. Heermance, and C. S. Wang (2005), Quaternary detachment folding of the Mingyaole anticline, southwestern Tianshan (in Chinese), *Seismol. Geol.*, *27*, 530–547.

Chen, J., R. Heermance, D. W. Burbank, K. M. Scharer, J. Miao, and C. Wang (2007a), Quantification of growth and lateral propagation of the Kashi anticline, southwest Chinese Tian Shan, *J. Geophys. Res.*, *112*, B03S16, doi:10.1029/2006JB004345.

Chen, Y.-G., K.-Y. Lai, Y.-H. Lee, J. Suppe, W.-S. Chen, Y.-N. N. Lin, Y. Wang, J.-H. Hung, and Y.-T. Kuo (2007b), Coseismic fold scarps and their kinematic behavior in the 1999 Chi-Chi earthquake Taiwan, *J. Geophys. Res.*, *112*, B03S02, doi:10.1029/2006JB004388.

Cheng, X., H. Chen, X. Lin, S. Yang, S. Chen, F. Zhang, K. Li, and Z. Liu (2016), Deformation geometry and timing of the Wupoer thrust belt in the NE Pamir and its tectonic implications, *Front. Earth Sci.*, *10*(4), 751–760, doi:10.1007/s11707-016-0606-z.

Coutand, I., M. R. Strecker, J. R. Arrowsmith, G. Hilley, R. C. Thiede, A. Korjenkov, and M. Omuraliev (2002), Late Cenozoic tectonic development of the intramontane Alai Valley, (Pamir-Tien Shan region, central Asia): An example of intracontinental deformation due to the Indo-Eurasia collision: Cenozoic development of the intramontane Alai Basin, *Tectonics*, *21*(6), 1053, doi:10.1029/2002TC001358.

Cowgill, E. (2010), Cenozoic right-slip faulting along the eastern margin of the Pamir salient, northwestern China, *Geol. Soc. Am. Bull.*, *122*(1–2), 145–161, doi:10.1130/B26520.1.

Daëron, M., J.-P. Avouac, and J. Charreau (2007), Modeling the shortening history of a fault tip fold using structural and geomorphic records of deformation, *J. Geophys. Res.*, *112*, B03S13, doi:10.1029/2006JB004460.

Dahlen, F. A. (1990), Critical taper model of fold-and-thrust belts and accretionary wedges, *Annu. Rev. Earth Planet. Sci.*, *18*, 55–99, doi:10.1146/annurev.ea.18.050190.000415.

Dahlen, F. A., J. Suppe, and D. Davis (1984), Mechanics of fold-and-thrust belts and accretionary wedges: Cohesive Coulomb Theory, *J. Geophys. Res.*, *89*, 10,087–10,101, doi:10.1029/JB089iB12p10087.

Dahlstrom, C. D. A. (1970), Structural geology of the eastern margin of the Canadian Rocky Mountains, *Bull. Can. Petrol. Geol.*, *18*(3), 332–406.

Dumitru, T. A., D. Zhou, E. Z. Chang, S. A. Graham, M. S. Hendrix, E. R. Sobel, and A. R. Carroll (2001), Uplift, exhumation, and deformation in the Chinese Tian Shan, *Mem.-Geol. Soc. Am.*, 71–100, doi:10.1130/0-8137-1194-0.71.

Engdahl, R. E., J. A. Jackson, S. C. Myers, E. A. Bergman, and K. Priestley (2006), Relocation and assessment of seismicity in the Iran region, *Geophys. J. Int.*, *167*(2), 761–778, doi:10.1111/j.1365-246X.2006.03127.x.

Erslev, E. A. (1991), Trishear fault-propagation folding, *Geology*, *19*(6), 617–620.

Farr, T. G., et al. (2007), The Shuttle Radar Topography Mission, *Rev. Geophys.*, *45*, RG2004, doi:10.1029/2005RG000183.

Frisch, W., L. Ratschbacher, M. R. Strecker, M. Waldhoer, V. Klischevich, M. Komilov, S. Semiletkin, and A. Zamoruyev (1994), Tertiary and Quaternary structures in the eastern Pamir, *J. Nepal Geol. Soc.*, *10*, 48–50.

Fu, B., Y. Ninomiya, and J. Guo (2010), Slip partitioning in the northeast Pamir–Tian Shan convergence zone, *Tectonophysics*, *483*(3–4), 344–364, doi:10.1016/j.tecto.2009.11.003.

Goode, J. K., D. W. Burbank, and B. Bookhagen (2011), Basin width control of faulting in the Naryn Basin, south-central Kyrgyzstan: Basin width control of faulting, *Tectonics*, *30*, TC6009, doi:10.1029/2011TC002910.

Goode, J. K., D. W. Burbank, and C. Ormukov (2014), Pliocene-Pleistocene initiation, style, and sequencing of deformation in the central Tien Shan, *Tectonics*, *33*, 464–484, doi:10.1002/2013TC003394.

Grützner, C., E. Carson, R. T. Walker, E. J. Rhodes, A. Mukambayev, D. Mackenzie, J. R. Elliott, G. Campbell, and K. Abdrakhmatov (2017), Assessing the activity of faults in continental interiors: Palaeoseismic insights from SE Kazakhstan, *Earth Planet. Sci. Lett.*, *459*, 93–104, doi:10.1016/j.epsl.2016.11.025.

He, P., Y. Wen, C. Xu, Y. Liu, and H. S. Fok (2015), New evidence for active tectonics at the boundary of the Kashi Depression, China, from time series InSAR observations, *Tectonophysics*, *653*, 140–148, doi:10.1016/j.tecto.2015.04.011.

Heermance, R. V., J. Chen, D. W. Burbank, and J. Miao (2008), Temporal constraints and pulsed Late Cenozoic deformation during the structural disruption of the active Kashi foreland, northwest China, *Tectonics*, *27*, TC6012, doi:10.1029/2007TC002226.

Hendrix, M. S., S. A. Graham, A. R. Carroll, E. R. Sobel, C. L. McKnight, B. J. Schulein, and Z. Wang (1992), Sedimentary record and climatic implications of recurrent deformation in the tian Shan: Evidence from Mesozoic strata of the north Tarim, south Junggar, and Turpan basins, northwest China, *Geol. Soc. Am. Bull.*, *104*(1), 53–79, doi:10.1130/0016-7606(1992)104<0053:SRACIO>2.3.CO;2.

Hendrix, M. S., T. A. Dumitru, and S. A. Graham (1994), Late Oligocene-early Miocene unroofing in the Chinese tian Shan: An early effect of the India-Asia collision, *Geology*, *22*(6), 487, doi:10.1130/0091-7613(1994)022<0487:LOEMUI>2.3.CO;2.

Huang, B., J. Piper, S. Peng, T. Liu, Z. Li, Q. Wang, and R. Zhu (2006), Magnetostratigraphic study of the Kuche Depression, Tarim Basin, and Cenozoic uplift of the Tian Shan Range, Western China, *Earth Planet. Sci. Lett.*, *251*(3–4), 346–364, doi:10.1016/j.epsl.2006.09.020.

Huang, B., J. D. A. Piper, and R. Zhu (2009), Paleomagnetic constraints on neotectonic deformation in the Kashi depression of the western Tarim Basin, NW China, *Int. J. Earth Sci.*, *98*(6), 1469–1488, doi:10.1007/s00531-008-0401-5.

Huang, W., X. Yang, A. Li, J. A. Thompson, and L. Zhang (2014), Climatically controlled formation of river terraces in a tectonically active region along the southern piedmont of the Tian Shan, NW China, *Geomorphology*, *220*, 15–29, doi:10.1016/j.geomorph.2014.05.024.

Hubert-Ferrari, A. (2005), Irregular earthquake cycle along the southern Tianshan front, Aksu area, China, *J. Geophys. Res.*, *110*, B06402, doi:10.1029/2003JB002603.

Hubert-Ferrari, A., J. Suppe, R. Gonzalez-Mieres, and X. Wang (2007), Mechanisms of active folding of the landscape (southern Tian Shan, China), *J. Geophys. Res.*, *112*, B03S09, doi:10.1029/2006JB004362.

Husson, L., J.-L. Mugnier, P. Leturmy, G. Vidal, and F. Cergy-Pontoise (2004), Kinematics and sedimentary balance of the sub-Himalayan zone, western Nepal, in *Thrust Tectonics and Hydrocarbon Systems*, *AAPG Memoir* vol. 82, edited by K. McClay, 115–130, Am. Assoc. of Pet. Geol., Houston, Tex.

Ischuk, A., et al. (2013), Kinematics of the Pamir and Hindu Kush regions from GPS geodesy, *J. Geophys. Res. Solid Earth*, *118*, 2408–2416, doi:10.1002/jgrb.50185.

Jordan, T. E., R. W. Allmendinger, J. F. Damanti, and R. E. Drake (1993), Chronology of motion in a complete Thrust Belt: The Precordillera, 30-31S, Andes Mountains, *J. Geol.*, *101*(2), 135–156.

Kao, H. (2000), The Chi-Chi earthquake sequence: Active, out-of-sequence thrust faulting in Taiwan, *Science*, *288*(5475), 2346–2349, doi:10.1126/science.288.5475.2346.

Koons, P. O., and E. Kirby (2007), Topography, denudation, and deformation: The role of surface processes in fault evolution, in *Tectonic Faults: Agents of Change on a Dynamic Earth*, edited by M. R. Handy, G. Hirth, and N. Hovius, pp. 205–230, MIT Press, Cambridge, MA.

Koons, P. O., P. K. Zeitler, C. P. Chamberlain, D. Craw, and A. S. Meltzer (2002), Mechanical links between erosion and metamorphism in Nanga Parbat, Pakistan Himalaya, *Am. J. Sci.*, *302*(9), 749–773.

Lave, J., and J. P. Avouac (2000), Active folding of fluvial terraces across the Siwaliks Hills, Himalayas of central Nepal, *J. Geophys. Res.*, *105*, 5735–5770.

Li, T. (2012), Active thrusting and folding along the Pamir Frontal Thrust System, China Earthquake Administration, PhD dissertation.

Li, T., J. Chen, J. A. Thompson Jobe, and D. W. Burbank (2017), Active flexural-slip faulting: Controls exerted by stratigraphy, geometry, and fold kinematics, *Journal of Geophysical Research: Solid Earth*, *122*, doi:10.1002/2017JB013966.

Li, T., J. Chen, J. A. Thompson, D. W. Burbank, and W. Xiao (2012), Equivalency of geologic and geodetic rates in contractional orogens: New insights from the Pamir frontal thrust, *Geophys. Res. Lett.*, *39*, L15305, doi:10.1029/2012GL051782.

Li, T., J. Chen, J. A. Thompson, D. W. Burbank, and X. Yang (2013), Quantification of three-dimensional folding using fluvial terraces: A case study from the Mushi anticline, northern margin of the Chinese Pamir, *J. Geophys. Res. Solid Earth*, *118*, 4628–4647, doi:10.1002/jgrb.50316.

Li, T., J. Chen, J. A. Thompson, D. W. Burbank, and X. Yang (2015a), Active flexural-slip faulting: A study from the Pamir-Tian Shan convergent zone, NW China, *J. Geophys. Res. Solid Earth*, *120*, 4359–4378, doi:10.1002/2014JB011632.

Li, T., J. Chen, J. A. Thompson, D. W. Burbank, and H. Yang (2015b), Hinge-migrated fold-scarp model based on an analysis of bed geometry: A study from the Mingyaole anticline, southern foreland of Chinese Tian Shan, *J. Geophys. Res. Solid Earth*, *120*, 6592–6613, doi:10.1002/2015JB012102.

Lisiecki, L. E., and M. E. Raymo (2005), A Pliocene-Pleistocene stack of 57 globally distributed benthic δ^{18}O records, *Paleoceanography*, *20*, PA1003, doi:10.1029/2004PA001071.

Lu, Y. C., X. L. Wang, and A. G. Wintle (2007), A new OSL chronology for dust accumulation in the last 130,000 yr for the Chinese Loess Plateau, *Quat. Res.*, *67*(1), 152–160, doi:10.1016/j.yqres.2006.08.003.

McCaffrey, R., M. D. Long, C. Goldfinger, P. C. Zwick, J. L. Nabelek, C. K. Johnson, and C. Smith (2000), Rotation and plate locking at the southern Cascadia subduction zone, *Geophys. Res. Lett.*, *27*, 3117–3120.

McClay, K., J.-A. Muñoz, and J. García-Senz (2004), Extensional salt tectonics in a contractional orogen: A newly identified tectonic event in the Spanish Pyrenees, *Geology*, *32*(9), 737–740.

Mohadjer, S. et al. (2010), Partitioning of India-Eurasia convergence in the Pamir-Hindu Kush from GPS measurements, *Geophys. Res. Lett.*, *37*, L04305, doi:10.1029/2009GL041737.

Molnar, P., and P. England (1990), Late Cenozoic uplift of mountain ranges and global climate change: Chicken or egg?, *Nature*, *346*, 29–34.

Mugnier, J.-L., P. Huyghe, P. Leturmy, and F. Jouanne (2004), Episodicity and rates of thrust-sheet motion in the Himalayas (western Nepal), in *Thrust Tectonics and Hydrocarbon Systems*, *AAPG Memoir 82*, edited by K. McClay, pp. 91–114, Am. Assoc. of Pet. Geol, Houston, Tex.

Murphy, M. A., M. H. Taylor, J. Gosse, C. R. P. Silver, D. M. Whipp, and C. Beaumont (2013), Limit of strain partitioning in the Himalaya marked by large earthquakes in western Nepal, *Nat. Geosci.*, *7*(1), 38–42, doi:10.1038/ngeo2017.

Negredo, A. M., A. Replumaz, A. Villaseñor, and S. Guillot (2007), Modeling the evolution of continental subduction processes in the Pamir–Hindu Kush region, *Earth Planet. Sci. Lett.*, *259*(1–2), 212–225, doi:10.1016/j.epsl.2007.04.043.

Nilforoushan, F., et al. (2003), GPS network monitors the Arabia-Eurasia collision deformation in Iran, *J. Geod.*, *77*(7–8), 411–422, doi:10.1007/s00190-003-0326-5.

Pan, B., D. Burbank, Y. Wang, G. Wu, J. Li, and Q. Guan (2003), A 900 ky record of strath terrace formation during glacial-interglacial transitions in northwest China, *Geology*, *31*(11), 957–960.

Pavlis, T. L., M. W. Hamburger, and G. L. Pavlis (1997), Erosional processes as a control on the structural evolution of an actively deforming fold and thrust belt: An example from the Pamir–Tien Shan region, central Asia, *Tectonics*, *16*, 810–822.

Poblet, J., and K. McClay (1996), Geometry and kinematics of single-layer detachment folds, *AAPG Bull.*, *80*, 1085–1109.

Qiao, X., P. Yu, Z. Nie, J. Li, X. Wang, S. I. Kuzikov, Q. Wang, and S. Yang (2017), The crustal deformation revealed by GPS and InSAR in the northwest corner of the Tarim Basin, northwestern China, *Pure Appl. Geophys.*, *174*(3), 1405–1423, doi:10.1007/s00024-017-1473-6.

Reilinger, R., et al. (2006), GPS constraints on continental deformation in the Africa-Arabia-Eurasia continental collision zone and implications for the dynamics of plate interactions, *J. Geophys. Res.*, *111*, B05411, doi:10.1029/2005JB004051.

Robinson, A. C., A. Yin, C. E. Manning, T. M. Harrison, S.-H. Zhang, and X.-F. Wang (2004), Tectonic evolution of the northeastern Pamir: Constraints from the northern portion of the Cenozoic Kongur Shan extensional system, western China, *Geol. Soc. Am. Bull.*, *116*(7), 953, doi:10.1130/B25375.1.

Robinson, A. C., A. Yin, C. E. Manning, T. M. Harrison, S. H. Zhang, and X.-F. Wang (2007), Cenozoic evolution of the eastern Pamir: Implications for strain-accommodation mechanisms at the western end of the Himalayan-Tibetan orogen, *Geol. Soc. Am. Bull.*, *119*(7–8), 882–896, doi:10.1130/B25981.1.

Rockwell, T. K., E. A. Keller, M. N. Clark, and D. L. Johnson (1984), Chronology and rates of faulting of Ventura River terraces, California, *Geol. Soc. Am. Bull.*, *95*(12), 1466, doi:10.1130/0016-7606(1984)95<1466:CAROFO>2.0.CO;2.

Scharer, K. M., D. W. Burbank, J. Chen, R. J. Weldon, C. Rubin, R. Zhao, and J. Shen (2004), Detachment folding in the Southwestern ian Shan–Tarim foreland, China: Shortening estimates and rates, *J. Struct. Geol.*, *26*(11), 2119–2137, doi:10.1016/j.jsg.2004.02.016.

Scharer, K. M., D. W. Burbank, J. Chen, and R. J. Weldon (2006), Kinematic models of fluvial terraces over active detachment folds: Constraints on the growth mechanism of the Kashi-Atushi fold system, Chinese Tian Shan, *Geol. Soc. Am. Bull.*, *118*(7–8), 1006–1021.

Schurr, B., L. Ratschbacher, C. Sippl, R. Gloaguen, X. Yuan, and J. Mechie (2014), Seismotectonics of the Pamir, *Tectonics*, *33*, 1501–1518, doi:10.1002/2014TC003576.

Schwab, M., et al. (2004), Assembly of the Pamirs: Age and origin of magmatic belts from the southern Tien Shan to the southern Pamirs and their relation to Tibet, *Tectonics*, *23*, TC4002, doi:10.1029/2003TC001583.

Seeber, L., and A. Pecher (1998), Strain partitioning along the Himalayan arc and the Nanga Parbat antiform, *Geology*, *26*(9), 791–794.

Seeber, L., J. G. Armbruster, and R. C. Quittmeyer (1981), Seismicity and continental subduction in the Himalayan arc, in *Zagros Hindu Kush Himalaya Geodynamic Evolution*, *Geodyn. Ser*, vol. 3, edited by H. K. Gupta and F. M. Delany, pp. 215–242, AGU, Washington D. C.

Shen, J., R. Zhao, J. Li, D. W. Burbank, and K. M. Scharer (2001), Measurements of terrace deformation and crustal shortening rate in the northwest margin of Tarim Basin, *Chin. Sci. Bull.*, *46*, 334–338.

Siame, L. L., O. Bellier, M. Sébrier, and M. Araujo (2005), Deformation partitioning in flat subduction setting: Case of the Andean foreland of western Argentina (28°S–33°S), *Tectonics*, *24*, TC5003, doi:10.1029/2005TC001787.

Sobel, E., J. Chen, and R. Heermance (2006), Late Oligocene–Early Miocene initiation of shortening in the southwestern Chinese Tian Shan: Implications for Neogene shortening rate variations, *Earth Planet. Sci. Lett.*, *247*(1–2), 70–81, doi:10.1016/j.epsl.2006.03.048.

Sobel, E. R., and T. A. Dumitru (1997), Exhumation of the margins of the western Tarim basin during the Himalayan orogeny, *J. Geophys. Res.*, *102*, 5043–5064, doi:10.1029/96JB03267.

Sobel, E. R., L. M. Schoenbohm, J. Chen, R. Thiede, D. F. Stockli, M. Sudo, and M. R. Strecker (2011), Late Miocene–Pliocene deceleration of dextral slip between Pamir and Tarim: Implications for Pamir orogenesis, *Earth Planet. Sci. Lett.*, *304*(3–4), 369–378, doi:10.1016/j.epsl.2011.02.012.

Sobel, E. R., J. Chen, L. M. Schoenbohm, R. Thiede, D. F. Stockli, M. Sudo, and M. R. Strecker (2013), Oceanic-style subduction controls late Cenozoic deformation of the Northern Pamir orogen, *Earth Planet. Sci. Lett.*, *363*, 204–218, doi:10.1016/j.epsl.2012.12.009.

Stearns, M. A., B. R. Hacker, L. Ratschbacher, D. Rutte, and A. R. C. Kylander-Clark (2015), Titanite petrochronology of the Pamir gneiss domes: Implications for middle to deep crust exhumation and titanite closure to Pb and Zr diffusion, *Tectonics*, *34*, 784–802, doi:10.1002/2014TC003774.

Suppe, J. (1983), Geometry and kinematics of fault-bend folding, *Am. J. Sci.*, *283*(7), 684–721, doi:10.2475/ajs.283.7.684.

Thiede, R. C., E. R. Sobel, J. Chen, L. M. Schoenbohm, D. F. Stockli, M. Sudo, and M. R. Strecker (2013), Late Cenozoic extension and crustal doming in the India-Eurasia collision zone: New thermochronologic constraints from the NE Chinese Pamir, *Tectonics*, *32*, 763–779, doi:10.1002/tect.20050.

Thompson, J. A. (2013), Neogene tectonic evolution of the NE Pamir margin, PhD Dissertation, UC Santa Barbara.

Thompson, J. A., D. W. Burbank, T. Li, J. Chen, and B. Bookhagen (2015), Late Miocene northward propagation of the northeast Pamir thrust system, northwest China, *Tectonics*, *34*, 510–534, doi:10.1002/2014TC003690.

Thompson, S. C., R. J. Weldon, C. M. Rubin, K. Abdrakhmatov, P. Molnar, and G. W. Berger (2002), Late Quaternary slip rates across the central Tien Shan, Kyrgyzstan, central Asia, *J. Geophys. Res.*, *107*(B9), 2203, doi:10.1029/2001JB000596.

Vázquez, F. R., C. H. Costa, and C. E. Gardini (2016), Quaternary-active thrusts scarps tested as deformation markers by trishear models in the Southern Precordillera of Argentina, *Quat. Int.*, doi:10.1016/j.quaint.2016.06.020.

Wang, C., X. Cheng, H. Chen, W. Ding, X. Lin, L. Wu, K. Li, J. Shi, and Y. Li (2016), The effect of foreland palaeo-uplift on deformation mechanism in the Wupoer fold-and-thrust belt, NE Pamir: Constraints from analogue modelling, *J. Geodyn.*, *100*, 115–129, doi:10.1016/j.jog.2016.03.001.

Whipple, K. X. (2009), The influence of climate on the tectonic evolution of mountain belts, *Nat. Geosci.*, *2*(2), 97–104.

Windley, B. F., M. B. Allen, C. Zhang, Z.-Y. Zhao, and G.-R. Wang (1990), Paleozoic accretion and Cenozoic redeformation of the Chinese Tien Shan Range, central Asia, *Geology*, *18*(2), 128, doi:10.1130/0091-7613(1990)018<0128:PAACRO>2.3.CO;2.

Wright, T. J. (2004), InSAR observations of low slip rates on the major faults of western Tibet, *Science*, *305*(5681), 236–239, doi:10.1126/science.1096388.

Xinjiang Bureau of Geology and Mineral Resources (1993), *Regional Geology of the Xinjiang Uygur Autonomous Region*, p. 561, Geol. Publ. House, Beijing.

Xinlu, S., C. Xinwei, W. Chao, and L. Jinhai (2004), Cenozoic thrust structures in the Kashi area, western Tarim Basin, *Chin. J. Geol.*, *39*(4), 543–550.

Xue, C., G. Chi, Z. Li, and X. Dong (2014), Geology, geochemistry and genesis of the cretaceous and Paleocene sandstone- and conglomerate-hosted Uragen Zn–Pb deposit, Xinjiang, China: A review, *Ore Geol. Rev.*, *63*, 328–342, doi:10.1016/j.oregeorev.2014.06.005.

Yang, H. L. (2013), Optical dating research of rapidly deposited sediments related to earthquakes. China Earthquake Administration. PhD Dissertation.

Yue, L.-F., J. Suppe, and J.-H. Hung (2011), Two contrasting kinematic styles of active folding above thrust ramps, Western Taiwan, in *Thrust Fault-Related Folding*, *AAPG Memoir*, vol. 94, edited by K. McClay, J. Shaw, and J. Suppe, pp. 153–186, Am. Assoc. Pet. Geol, Okla.

Zeitler, P. K., P. O. Koons, M. P. Bishop, C. P. Chamberlain, D. Craw, M. A. Edwards, S. Hamidullah, M. Q. Jan, M. Khattak, and W. S. Kidd (2001), Crustal reworking at Nanga Parbat, Pakistan: Metamorphic consequences of thermal-mechanical coupling facilitated by erosion, *Tectonics*, *20*, 712–728.

Zhou, Y., J. He, I. Oimahmadov, M. Gadoev, Z. Pan, W. Wang, S. Abdulov, and N. Rajabov (2016), Present-day crustal motion around the Pamir Plateau from GPS measurements, *Gondwana Res.*, *35*, 144–154, doi:10.1016/j.gr.2016.03.011.

Zubovich, A., T. Schöne, S. Metzger, O. Mosienko, S. Mukhamediev, A. Sharshebaev, and C. Zech (2016), Tectonic interaction between the Pamir and Tien Shan observed by GPS, *Tectonics*, *35*, 283–292, doi:10.1002/2015TC004055.

Zubovich, A. V. et al. (2010), GPS velocity field for the Tien Shan and surrounding regions, *Tectonics*, *29*, TC6014, doi:10.1029/2010TC002772.